Stacking fault energy and microstructure effects on torsion texture evolution

By Darcy A. Hughes[1], Ricardo A. Lebensohn[2],
Hans Rudolf Wenk[3] and Ashish Kumar[4]

[1]Center for Materials and Applied Mechanics, Sandia National Laboratories,
Livermore, CA 94550, USA
[2]Instituto de Fisica Rosario (CONICET-UNR) 2000, Rosario, Argentina
[3]Department of Geology, University of California, Berkeley, CA 94720, USA
[4]Division of Engineering, Brown University, Providence, RI 02912, USA

A series of experiments and simulations that vary the texture and microstructure simultaneously are used to establish the role of the microstructure in texture formation in FCC metals. The stacking fault energy (SFE) of the metal, which is known to have a strong impact on texture and microstructure, is the vital parameter used to make these variations. It was determined that the wide variety of textures and microstructures observed as a function of SFE and temperature was developed by slip processes alone; twinning was not necessary, as previously thought. The different textures are caused by (i) variations in local slip patterns within a single grain, as revealed by grain subdivision into differently deforming cell blocks; and (ii) more subtly by the cell-block shape. The local selection of slip systems creating the lattice rotations within a cell block is altered by the planarity of slip. Slip planarity is controlled by the SFE and temperature. It is hypothesized that the new texture components, that are distinct from the generally accepted ideal components, are created by the different slip processes occurring as a result of low SFE and low temperature. A more subtle effect of grain subdivision is related to the cell-block shapes that develop as a function of SFE and temperature and correspond to the different textures observed. The shape of the cell block is related to the level of constraint required by the deformation. The slip pattern changes and cell-block shapes correlate with the presence or absence of certain ideal texture components whose evolution is not simulated. Materials and conditions with similar deformation microstructures developed similar textures in the experiments.

Keywords: texture; microstructure; twinning; dislocations;
stacking fault energy; torsion

1. Introduction

The formation of a preferred crystallographic texture during deformation has been studied extensively in the past through both experimental measurement and computer simulation (see, for example, Williams 1962; van Houtte & Aernoudt 1976; Gil Sevillano et al. 1980; Sekine et al. 1981; Hecker & Stout 1982; Canova et al. 1984; Montheillet et al. 1984; Stout et al. 1988; Harren et al. 1989; Stout & O'Rourke 1989; Toth et al. 1989). Significant advances in texture simulation have occurred

Proc. R. Soc. Lond. A (2000) **456**, 921–953

921

in the last 20 years (Kocks *et al*. 1998), including variations of the Taylor model (Taylor 1938), e.g. the full-constraints (FC) model (van Houtte & Aernoudt 1976; Canova *et al*. 1984; Harren *et al*. 1989; Toth *et al*. 1989), the relaxed-constraints (RC) model (Honneff & Mecking 1981; Canova *et al*. 1984), the self-consistent model (Molinari *et al*. 1987; Tomé & Canova 1998; Lebensohn & Tomé 1993), and finite-element based schemes (e.g. Becker 1991; Bronkhorst *et al*. 1992; Beaudoin *et al*. 1995). However, discrepancies still exist between the measured texture evolution and the simulation results (Stout *et al*. 1988). Notable among these differences are the presence or absence of certain ideal components, different ratios of ideal texture components as a function of strain, a much slower texture evolution in experiment than model, and the spread of orientations around the ideal components that is related to the intensity of a preferred orientation. These differences have remained over the years, despite the introduction of different types of models. In these models, with the exception of some finite-element (e.g. Beaudoin *et al*. 1996; Becker 1995) and *n*-site self-consistent approaches (see, for example, Canova *et al*. 1992), the slip pattern is modelled across a whole grain and the microstructural changes relate only to grain shape, and, possibly, to twinning. Consequently, a radical new approach may be required to resolve these issues. One such approach may be to consider the evolution of the deformation-induced dislocation microstructures, which takes place simultaneously with the texture evolution. This approach is introduced because the dislocation structure both reflects and modifies the slip pattern, thereby altering the texture development.

Before the microstructure can be included in a texture simulation, however, the role of the microstructure must be established by a simultaneous and careful consideration of the measured texture, texture simulations and quantitative observations of the dislocation structure. It is the aim of this paper to make this connection through a series of experiments and simulations that varies the texture and microstructure simultaneously. The vital parameter of choice to make these variations is the stacking fault energy (SFE) of the metal, which is known to have a strong impact on texture and microstructure. For the different SFEs, the range of possible texture and microstructure combinations is further increased by changing the temperature.

To further clarify the impact of the SFE on texture and microstructures, torsion deformation is examined. In torsion, with its dyadic symmetry (only one twofold symmetry axis), the effect of low SFE on the texture development is especially evident due to the formation of one special texture component, $(111)[1\bar{1}2]$, that is generally either lacking or very weak in the texture developed by the high-SFE metals (van Houtte & Aernoudt 1976; Gil Sevillano *et al*. 1980). Torsion has other advantages over rolling in trying to ascertain the various roles of the slip pattern and twinning. Stress-induced deformation twinning is postponed to larger strains in torsion, since flow stresses are lower in torsion, thereby allowing the texture to form by slip prior to twinning. Shear banding is very minimal in torsion, but would add complications to a similar analysis of texture during rolling.

The outline of the paper is as follows. First, the experimental textures are presented as a function of SFE and increasing strain for pure nickel and nickel–cobalt solid solutions. Next, the simulated textures are described including the assumptions and parameters used to vary the texture in the simulations. Both Taylor and self-consistent models are used. A step-by-step comparison is made with experiment to see what can and cannot be explained currently by the simulations. Finally, the

Table 1. *Materials and deformation conditions*

material	stacking fault energy[a] (mJ m^{-2})	initial recrystallized grain size[b] (μm)	starting texture	shear strain $\gamma_{z\theta}$	von Mises equivalent strain ε_{vM}	temperature (K)
nickel (99.99%)	240	80	random	2.0	1.2	296
				3.6	2.1	
				6.9	4.0	
				3.7	2.1	573
Ni + 30 wt% Co	150	53	random	1.9	1.1	296
				3.8	2.2	
				8.3	4.8	
Ni + 60 wt% Co	20	44	random	2.0	1.2	296
				3.2	1.8	
				5.8	3.6	
				3.8	2.2	573

[a] Beeston *et al.* (1968).
[b] Heyn intercept distance.

microstructures are described and discussed with respect to their influence on texture formation. Brief summaries and explanations are used in the text to aid the reader and maintain a connection between these diverse areas.

2. Experimental procedures

Three metals with a wide range of SFEs were studied: high-purity nickel (99.99%), Ni + 30 wt% Co and Ni + 60 wt% Co (see table 1). Cobalt additions to nickel systematically lower the SFE (Beeston *et al.* 1968) and, consequently, change the deformation behaviour with increasing cobalt concentration. Other contributions to behaviour changes, such as solid solution hardening, are minimized because nickel and cobalt have very similar atomic sizes, elastic moduli and melting temperatures. Constant strain rate torsion tests, $\gamma_{z\theta} = 10^{-3} \text{ s}^{-1}$, were performed at room temperature and 573 K using short thin-walled tube samples; the deformation conditions are outlined in detail in Hughes & Nix (1989). All samples were recrystallized prior to testing. It was ascertained from pole figure measurements that the starting texture was random. The starting material parameters and deformation conditions are listed in table 1 for the three materials.

Texture and microscopy samples were prepared from the starting materials and from the torsion samples following deformation. Optical metallography showed that these materials initially had equiaxed medium-large sized grains (table 1). Additionally, recrystallized grains in both Ni + 30 wt% Co and Ni + 60 wt% Co contained annealing twins, whereas pure nickel had very few annealing twins, consistent with their SFEs (Hughes & Nix 1988).

Texture samples were made from the ring-shaped gauge section of torsion samples, which were cut into segments, unrolled, assembled to increase the surface area, mechanically polished and electropolished. The surface of the texture samples corresponds to the $z\theta$-plane of the torsion sample. Throughout the text, z refers to the

Table 2. *Ideal texture components for FCC torsion (see also figures 1h and 2h)*

label	crystal orientation $\{hkl\}\langle uvw \rangle$[a]
A_1^*	$(111)[2\bar{1}\bar{1}]$
A_2^*	$(\bar{1}11)[211]$
A	$\{111\}\langle 1\bar{1}0 \rangle$
B	$\{112\}\langle 1\bar{1}0 \rangle$
C	$\{001\}\langle 1\bar{1}0 \rangle$
$\{111\}$ fibre	$\{111\}\langle uvw \rangle$
$\langle 110 \rangle$ fibre	$\{hkl\}\langle 110 \rangle$

[a] The designation $\{hkl\}\langle uvw \rangle$ refers to the shear plane and shear direction, respectively, for torsion.

shear plane normal, θ to the maximum shear direction, and r to the radial direction of the torsion sample. Conventional X-ray techniques in reflection geometry were used to measure incomplete (111), (200) and (220) pole figures. Fe Kα radiation was used to avoid fluorescence from cobalt. The intensity data were corrected for background and defocusing. The orientation distribution functions (ODFs) were calculated from incomplete pole figures using WIMV (Williams–Imhof–Matthies–Vinel) implemented in Beartex (Wenk *et al.* 1998). Crystal ODFs are represented in Rodrigues space (Frank 1988). Volume fractions of the various ideal texture components (shown in table 2) were calculated from the ODFs using a three-dimensional angular spread of 15° about an ideal component. These ideal texture components are labelled according to the nomenclature of Montheillet *et al.* (1984).

Transmission electron microscopy (TEM) analysis was performed on samples made in the $z\theta$-plane, which contains the maximum shear strain. Orientations of individual crystallites were obtained in the TEM from convergent-beam Kikuchi patterns. The Kikuchi patterns were analysed using a computer method based on Young *et al.* (1973) and Liu (1994) to obtain orientation matrices for individual crystallites. The minimum angle misorientation relationship (disorientation) between adjacent crystallites separated by dislocation boundaries was calculated by considering all 24 symmetry operations for the orientation matrices in a standard manner. The angle–axis pairs for the disorientations were also calculated. A negative or positive disorientation angle was assigned by considering whether the disorientation axis is in a left-hand or right-hand triangle, respectively.

3. Measured texture results

In the following section, the experimental textures are quantified by using ODFs. The ODF relates the orientation of the crystallographic axes to the macroscopic sample axes and is plotted in orientation space (i.e. Euler space). For symmetric crystals, such as the current cubic case, the whole of orientation space contains much redundant information. As a result, crystal symmetry is frequently used to reduce the orientation space to a fundamental region in which these redundancies are removed (or nearly removed). Herein, instead of the Euler angle spaces conventionally employed in texture analysis, Rodrigues space is used. The advantages and use of Rodrigues space have been discussed by various authors (see, for example, Frank

1988; Becker & Panchanadeeswaran 1989; Kumar & Dawson 1995). For example, texture comparisons are particularly convenient because the inherent symmetry of the space relates the axes of the space directly to the sample axes. Also, most ideal components of the torsion texture lie either on, or close to, the surface (or boundary) of the cubic fundamental region. As a result, the structures of the textures developed can be inferred from single plots of the ODF on the surface of the fundamental region. Because the ideal components and fibre textures created by the deformation lie on or near the surface, these presentations of the ODF can be readily interpreted like pole figures. In contrast to pole figures, the three-dimensional information is more distinctly retained. Note, however, that some minor components and recrystallization components may lie inside the fundamental region. The absence or presence of these components should be checked by cross-sectioning the space. Cross-sectioning in the present case did not reveal any minor components lying inside the space. Thus, the surface plots of the cubic fundamental region are representative.

Figure 1 displays complete {111} pole figures recalculated from the ODF for all samples. The maximum pole density observed is 3.26 multiples of a random distribution, whereas the minimum is 0.23. (The pole figure for nickel at the smallest strain shows several spurious maxima. They are attributed to regions of rather coarse grain size and small sample dimensions.) All textures display a statistical monoclinic symmetry with a dyad parallel to the radial direction, in accordance with the torsion deformation geometry. The pole figures illustrate considerable variation in textures consistent with changes in SFE (cobalt content), temperature and strain. These changes will be described with respect to the ideal orientations.

The ideal orientations for torsion texture development listed in table 2 have been plotted in both a pole (figure 1) and in Rodrigues space (figure 2) to aid the reader. Different ideal torsion textures include the development of orientations with the slip plane parallel to the shear plane along the $\{111\}\langle uvw \rangle$ fibre that includes the components A $\{111\}\langle 1\bar{1}0 \rangle$, A_1^* $(111)[2\bar{1}\bar{1}]$ and A_2^* $(\bar{1}11)[211]$. This {111} fibre may be present as only a partial fibre in which orientations near either A_1^* or A_2^* are missing, thus creating the monoclinic dyadic symmetry of figure 1a, d, e, i–l. A second common fibre forms in which the slip direction $\langle 110 \rangle$ is parallel to the shear direction. Orientations in this fibre include the B $\{112\}\langle 1\bar{1}0 \rangle$, C $\{001\}\langle 1\bar{1}0 \rangle$ and A $\{111\}\langle 1\bar{1}0 \rangle$ components. Note that A is common to both {111} and $\langle 110 \rangle$ fibres. Additionally, the C and A_1^* and A_2^* components are linked together through the macroscopic spin in the radial $\langle 110 \rangle$ direction. Rodrigues space is particularly useful in distinctly separating these various components, many of which blur together on a pole figure.

The ODFs for the three materials (SFEs) with increasing values of strain and temperature are plotted in figure 2. Figure 2 shows that well-formed torsion textures have already developed even at the lowest strain for all of the materials at both temperatures. The relative volume fractions, V_f (figure 3) of orientations associated with the ideal components depends on the material (SFE) and temperature and evolves with strain.

For the high-to-medium SFE tests conducted at 296 K, there is a close similarity in the texture development for the nickel and Ni + 30 wt% Co (table 3 and figure 2a–g). The only difference is the consistently higher intensities and volume fractions of the A and B components in nickel compared with Ni + 30 wt% Co. At all of the strain levels measured, the volume fractions of orientations are fairly well divided between the A, B and C components in nickel and Ni + 30 wt% Co (figure 3). (The
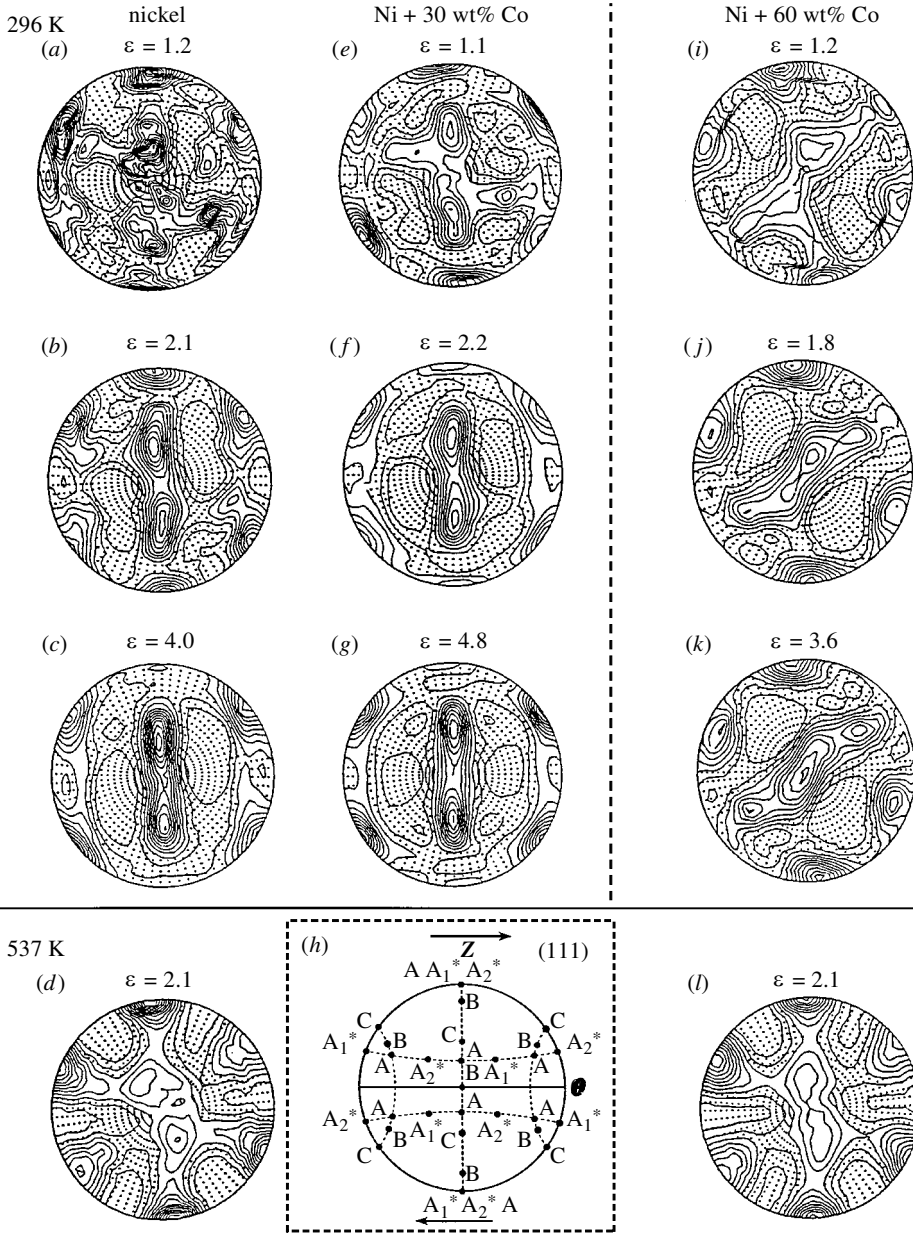
Figure 1. Experimental {111} pole figures in equal area projections showing the texture transition with increasing strain, decreasing SFE and increasing temperature. (a) Nickel, 296 K, $\varepsilon_{vM} = 1.2$; (b) nickel, 296 K, $\varepsilon_{vM} = 2.1$; (c) nickel, 296 K, $\varepsilon_{vM} = 4.0$; (d) nickel, 573 K, $\varepsilon_{vM} = 2.1$; (e) Ni + 30 wt% Co, 296 K, $\varepsilon_{vM} = 1.1$; (f) Ni + 30 wt% Co, 296 K, $\varepsilon_{vM} = 2.2$; (g) Ni + 30 wt% Co, 296 K, $\varepsilon_{vM} = 4.8$. (h) The locations of the ideal texture components are labelled according to the designations in table 2. (i) Ni + 60 wt% Co, 296 K, $\varepsilon_{vM} = 1.2$; (j) Ni + 60 wt% Co, 296 K, $\varepsilon_{vM} = 1.8$; (k) Ni + 60 wt% Co, 296 K, $\varepsilon_{vM} = 3.6$; (l) Ni + 60 wt% Co, 573 K, $\varepsilon_{vM} = 2.1$.
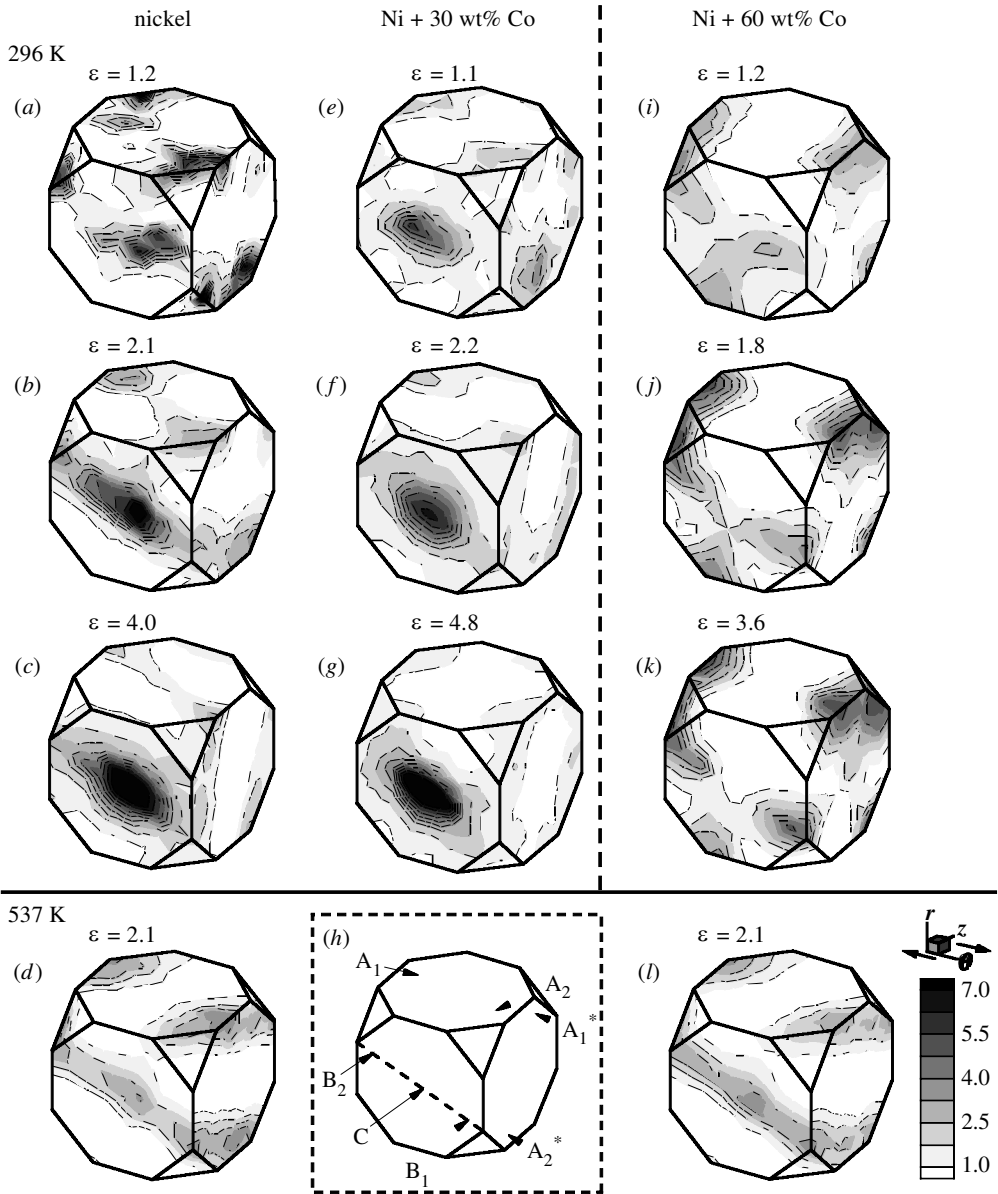
Figure 2. Some experimental ODFs plotted in Rodrigues space showing the texture transition with increasing strain, decreasing SFE and increasing temperature. (a) Nickel, 296 K, $\varepsilon_{\mathrm{vM}} = 1.2$; (b) nickel, 296 K, $\varepsilon_{\mathrm{vM}} = 2.1$; (c) nickel, 296 K, $\varepsilon_{\mathrm{vM}} = 4.0$; (d) nickel, 573 K, $\varepsilon_{\mathrm{vM}} = 2.1$; (e) Ni + 30 wt% Co, 296 K, $\varepsilon_{\mathrm{vM}} = 1.1$; (f) Ni + 30 wt% Co, 296 K, $\varepsilon_{\mathrm{vM}} = 2.2$; (g) Ni + 30 wt% Co, 296 K, $\varepsilon_{\mathrm{vM}} = 4.8$. (h) The locations of the ideal texture components in the fundamental region are labelled according to the designations in table 2. Note that the angular distance of the dashed line from corner to corner is 90°. (i) Ni + 60 wt% Co, 296 K, $\varepsilon_{\mathrm{vM}} = 1.2$; (j) Ni + 60 wt% Co, 296 K, $\varepsilon_{\mathrm{vM}} = 1.8$. Note that the intensities that peak around the bottom corner of the left face are part of the fibre running between A$_2^*$ and B. (k) Ni + 60 wt% Co, 296 K, $\varepsilon_{\mathrm{vM}} = 3.6$; (l) Ni + 60 wt% Co, 573 K, $\varepsilon_{\mathrm{vM}} = 2.1$.
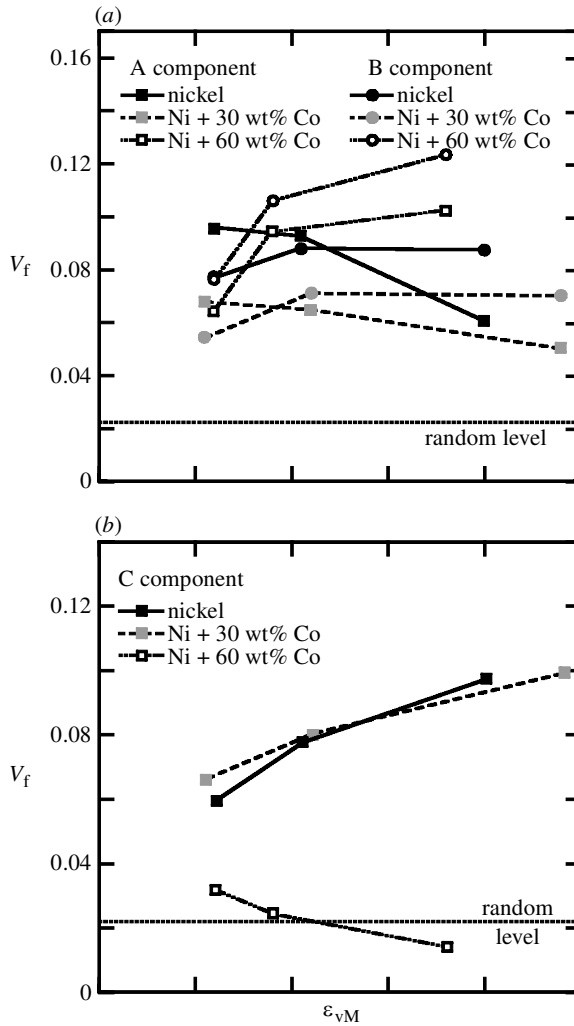
Figure 3. Volume fractions of the texture components with increasing strain for the three materials: (*a*) A and B components; (*b*) C component.

special A^* components will be discussed at the end of this section.) While the A and B components are the stronger components from $\varepsilon_{vM} = 1.2$–2.2 in terms of both volume fractions (figure 3) and peak intensities (figure 2), the C component becomes the strongest at $\varepsilon_{vM} = 4$. Both the B and C components increase with increasing strain (figure 3*a*, *b*), albeit this increase is much stronger for the C component. As shown in the ODFs, orientations are strongly spread in a short fibre $\langle 110 \rangle$ from C towards B at all strain levels.

Overall, except for the A and B components, the texture development for the low-SFE Ni + 60 wt% Co at 296 K is very different. A very weak C component forms and disappears below random intensity with increasing strain. Uniquely, the low-SFE Ni + 60 wt% Co at 296 K develops a strong partial fibre between the A_1^*, B and A components that increases with increasing strain, as shown by the peak intensi-
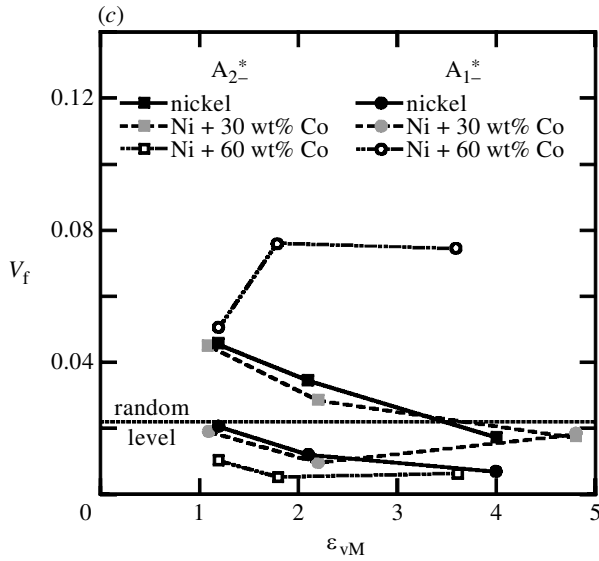
Figure 3. (*Cont.*) (*c*) A_1^* and A_2^* components.

Table 3. *Texture types observed in experiment as a function of material/SFE and temperature at intermediate-to-large strain*

material and temperature	intermediate strain		large strain	
	major ideal components	fibre textures	major ideal components	fibre textures
573 K: nickel and Ni + 60 wt% Co	A, B, C, A_1^*, A_2^*	complete $\{111\}\langle uvw\rangle$ $\{hkl\}\langle 110\rangle$	A, B, C, A_1^*, A_2^*	complete $\{111\}\langle uvw\rangle$ $\{hkl\}\langle 110\rangle$
296 K: nickel and Ni + 30 wt% Co	A, B, C, A_1^*	partial $\{111\}\langle uvw\rangle$ $\{hkl\}\langle 110\rangle$	C	partial $\{hkl\}\langle 110\rangle$
296 K: Ni + 60 wt% Co	A, B, A_1^*	partial A_2–B_2–A_1^*–A_1 fibres	A, B, A_1^*	partial A_2–B_2–A_1^*–A_1 fibres

ties (figure 2*i*–*k*) and volume fractions (figure 3). Note, importantly, that the peak intensities along this fibre are located 15–20° away from the exact location of the ideal components. This low-SFE texture may be better described by a new ideal component $\{\bar{5}45\}\langle 652\rangle$.

At the higher temperature of 573 K, all of the ODFs are similar and independent of either high or low SFE, e.g. nickel (figure 2*d*) and Ni + 60 wt% Co (figure 2*l*). These ODFs are characterized by long and wide fibre texture of moderate intensity that can be seen to wrap around the cubic fundamental region. This long fibre texture encompasses a uniform distribution of orientations connecting all of the A, B and C components along the $\langle 110\rangle$ fibre to the A_1^*, A_2^* and A along the $\{111\}$ fibre. This full fibre texture is in contrast to the dominance of a partial $\langle 110\rangle$ fibre strongly

centred at C for the lower temperature, 296 K, and large strain ODFs of nickel and Ni + 30 wt% Co (figure 2b, f).

While both A_1^* and A_2^* components are observed at 573 K regardless of SFE, the presence of either A_1^* or A_2^* depends on SFE at the lower temperature of 296 K. For high SFE, only a moderately weak A_2^* component is observed at low strain, which disappears at strains above $e = 1.2$ (figures 1a, e and 2a, e). For low SFE and temperature, no A_2^* is observed (figure 2i–k); instead, a moderate A_1^* is present at all strains.

Table 3 summarizes the different texture results as functions of material, SFE and temperature. Note the very large difference in texture components formed in the low-SFE metal at low temperature compared with medium-to-high SFE.

4. Polycrystal simulation

Deformation-induced texture development has been frequently explored by using models for polycrystal behaviour. The important factors of SFE and temperature generally enter into these models only as factors that activate twinning and change the hardening response. Two of these models will be considered herein as examples to help explain the experimental observations as well as the differences between simulations and experiment: an FC Taylor model and the self-consistent model (Lebensohn & Tomé 1993). These two models, like all models of polycrystal behaviour, are based on deriving polycrystal response from the collective response of a representative discrete aggregate of single crystals. Two components comprise a typical polycrystal model: a model for the mechanical response of individual crystals, and a homogenizing hypothesis to link the response of individual crystals to that of the polycrystal. The single-crystal model determines the way in which the applied deformation is partitioned among the participating accommodation mechanisms, such as elasticity, dislocation glide (slip), and twinning. This model then determines the stress developed in the single crystal as a consequence of this partitioning as well as its lattice rotations. That lattice rotation leads to the development of a preferred orientation of the crystal with increasing deformation. The evolving orientations of all the crystals provide the sample texture development. The homogenizing hypothesis, on the other hand, relates the stress and strain associated with individual crystals to that of the polycrystal by appropriate averaging. Hypotheses range from the Taylor FC hypothesis, which assumes that individual crystals experience the polycrystal deformation identically, to the Sachs hypothesis, which assumes that individual crystal stresses are equal to the polycrystal stress. The self-consistent hypothesis performs the homogenizing by embedding crystals in a homogeneous effective medium (HEM), representing the average properties of the polycrystal.

(a) Simulation results

In this section, we present and discuss predictions of torsion textures in FCC materials using Lebensohn & Tomé's (1993) implementation of the viscoplastic self-consistent (VPSC) model, as well as some Taylor FC results. Details of the simulation method are given in Appendix A. All the simulations shown here were performed using an initial random texture of 1000 grains. The active deformation mechanisms considered were the $\{111\}\langle110\rangle$ slip and the $\{111\}\langle112\rangle$ twinning (the latter has,

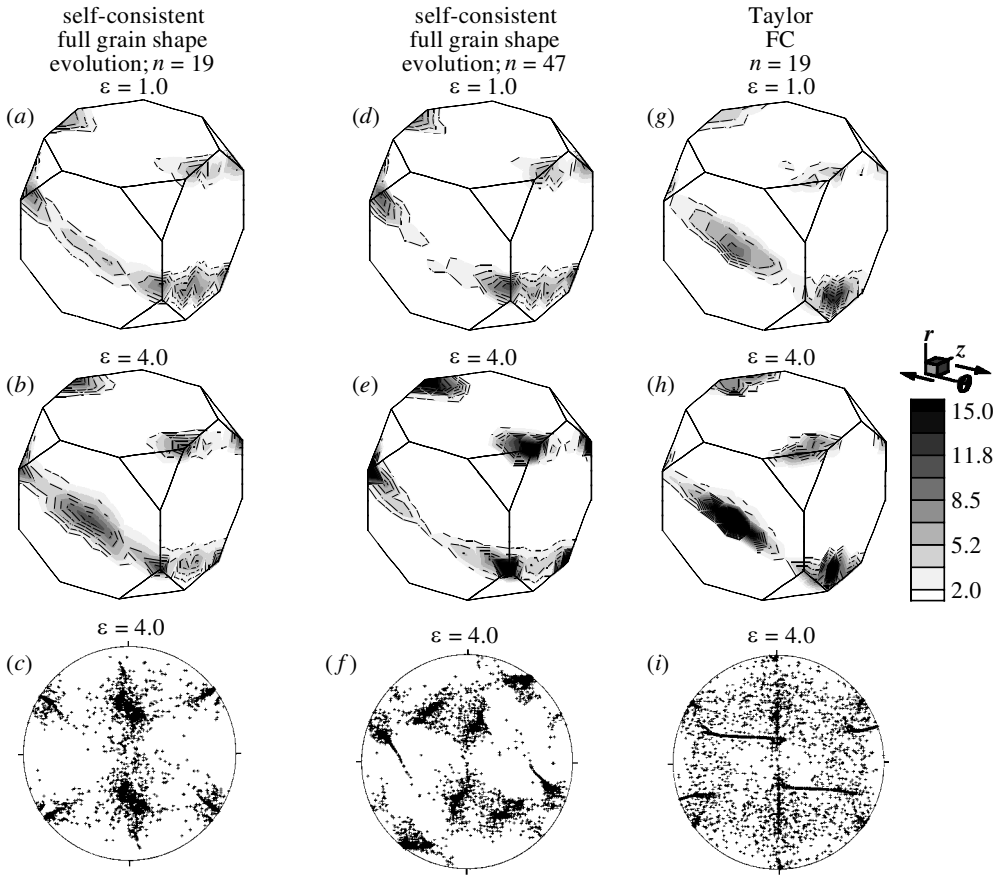Figure 4. Simulated ODFs plotted in Rodrigues space and {111} pole figures in equal area projections for the case of deformation by slip only. (*a*) VPSC model with grain-shape updating, inverse rate sensitivity $n = 19$, $\varepsilon_{vM} = 1$; (*b*) same as (*a*) with $\varepsilon_{vM} = 4$; (*c*) same as (*b*). (*d*) VPSC model with grain-shape updating, $n = 47$, $\varepsilon_{vM} = 1$; (*e*) same as (*d*) with $\varepsilon_{vM} = 4$; (*f*) same as (*d*). (*g*) FC Taylor model, $n = 19$, $\varepsilon_{vM} = 1$; (*h*) same as (*g*) with $\varepsilon_{vM} = 4$; (*i*) same as (*h*).

associated with it, a characteristic twin shear of 0.707). For those simulations that included twinning, the initial critical stresses of both slip and twinning were arbitrarily assumed to be equal (1.0 arbitrary units). The rules governing the evolution of the critical stresses with deformation are given in Appendix A. A total strain of $\varepsilon_{vM} = 4.0$ was imposed in incremental steps of $\varepsilon_{vM} = 0.01$. Both the final and certain interesting intermediate textures are presented and discussed. Some of these textures are shown as (111) pole figures, but, for most of them, we rely on the more transparent Rodrigues representation.

Different aspects of texture formation were investigated using the Taylor FC and the VPSC models, namely

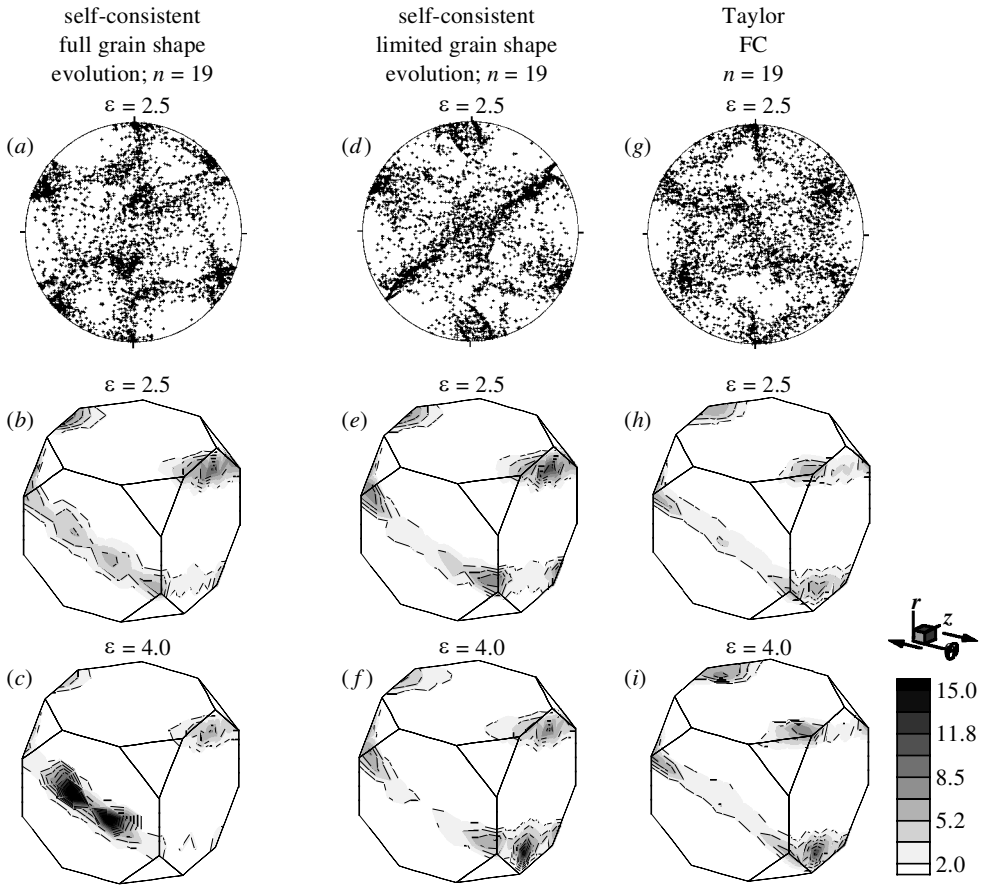(a) the presence or absence of twinning;

(b) the effect of rate sensitivity;

Figure 5. Simulated ODFs plotted in Rodrigues space and {111} pole figures in equal area projections for the case of deformation by slip and twinning. In all cases, the deformation consisted of an early stage (up to $\varepsilon_{vM} = 1$) of only slip and a late stage of slip plus twinning. (*a*) VPSC model with grain-shape updating, inverse rate sensitivity, $n = 19$, $h^{tw} = 0.1$, $\varepsilon_{vM} = 2.5$; (*b*) same as (*a*); (*c*) same as (*a*) for $\varepsilon_{vM} = 4$. (*d*) VPSC model without grain-shape updating, $n = 19$, $h^{tw} = 0.1$, $\varepsilon_{vM} = 2.5$; (*e*) same as (*d*); (*f*) same as (*d*) for $\varepsilon_{vM} = 4$. (*g*) FC Taylor model, $n = 19$, $h^{tw} = 0.1$, $\varepsilon_{vM} = 2.5$; (*h*) same as (*e*); (*i*) same as (*e*) $\varepsilon_{vM} = 4$.

(c) the effect of grain rotations by both slip and twinning;

(d) the influence of final amount of twinned volume fraction;

(e) the grain-shape effect as predicted by the VPSC model.

We use twinning to implicitly model one possible effect of temperature and SFE. In order to discuss these aspects, we present intermediate and final textures corresponding to the following cases.

1. *Only slip cases (figure 4).* Taylor FC and VPSC simulations for moderate rate sensitivity ($n = 1/m = 19$) and VPSC with low rate sensitivity ($n = 1/m = 47$).
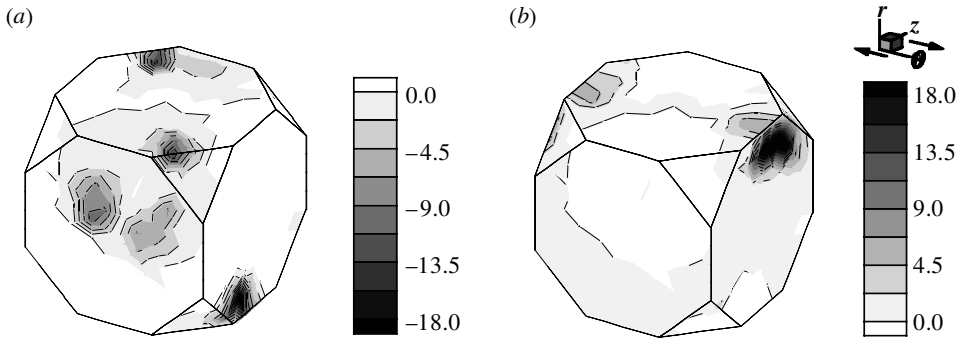
(a)

(b)

Figure 6. The ODFs showing the orientations of regions that twin in the simulations and their orientations after twinning. (a) Orientations near A_2^* preferentially twin. (b) All regions reoriented to A_1^* by twinning.

2. *Slip plus twinning cases with and without grain-shape updating (figure 5).* Taylor FC and VPSC simulations consisting of an early stage (up to $\varepsilon_{vM} = 1.0$) of only slip and a late stage of slip plus twinning (up to the final strain of $\varepsilon_{vM} = 4.0$), assuming $h^{tw} = 0.1$, regular grain-shape updating and moderate rate sensitivity ($n = 1/m = 19$), and same VPSC simulation but preventing grain-shape updating during the late stage.

In general, for the case of slip alone, both the Taylor FC and the VPSC models, with a moderate rate sensitivity, $n = 19$, predict the formation of the A_2^*, A, B and C components following moderate-to-large strains (figure 4a–c, g–i). The B component is stronger, relatively, in the VPSC simulation compared with the Taylor simulation, especially if the grain shape is not evolved in the VPSC model. For the case of Taylor, a strong partial $\{111\}$ fibre plus a weak $\langle 110 \rangle$ fibre connects the sharp peaks of these components (figure 4g, h), whereas a complete $\{111\}$ fibre plus a stronger $\langle 110 \rangle$ fibre connects these peaks in the VPSC case (figure 4a, b). This complete $\{111\}$ fibre contains both the A_1^* and A_2^* components in the VPSC simulation. Consequently, the VPSC model produces a texture that approaches orthotropic symmetry in contrast to the clear dyadic symmetry of the Taylor results.

The volume fraction of all the components increases with increasing strain from moderate to large strains. A transition in this trend occurs at large strains ($\varepsilon_{vM} = 3$, $n = 19$, VPSC) in which the C component increases rapidly with strain at the expense of the decreasing A, B and A_2^* components. The strain level at which this reversal occurs depends on the value of the rate sensitivity and on the grain shape. Decreasing the rate sensitivity significantly retards the formation of the C component to very large strains above 4, as shown by the strong B component and lack of C component in figure 4e compared with figure 4b. Decreasing the rate sensitivity also increases the texture peak intensities, weakens the connecting fibre textures, and changes the relative ratios of the intensity peaks of $A_1^*/C/A_2^*$ with strain. Grain shape retards or enhances the formation of the C component. If the grain shape is kept spherical in the simulations, then very little C component forms following $\varepsilon_{vM} \leqslant 4.0$.

If twinning was included in the simulations, twinning was suppressed below a strain of 1, which corresponds with the experimental observations. As the strain is increased above 1, the start of twinning enhances the formation of the opposite A_1^*

component and its adjacent partial {111} fibre at the expense of the A_2^* for both the VPSC and Taylor models with slip plus twinning (figure 5). In the simulation, grains that twinned had orientations near one of three types of orientation, all of which twinned to orientations near A_1^* and its adjacent partial {111} fibre. Those orientations associated with twinning, shown in figure 6, were A_2^*, regions on either side of the C component near the ⟨110⟩ fibre, and near $\{56\bar{4}\}\langle 7\bar{8}\bar{3}\rangle$. Thus, the increase in the A_1^* component with twinning is due primarily to the twinning of A_2^* and, to a lesser extent, to twinning of regions near C and $\{56\bar{4}\}\langle 7\bar{8}\bar{3}\rangle$. The density of orientations near both A_2^* and C diminishes for the case of twinning compared with just slip (compare figures 4b and 5b). With increasing strain, the amount of twinning tapers off as the critical stress of twinning, relative to slip, increases. For the present set of parameters, the final, stable, twinned volume fraction reached, in the VPSC case, a value of 28.9% at around 2.4 strain. Once the twin activity drops to a very low value, the orientations near the A_1^* component are not stable with respect to continued slip. Thus they rotate back to near the A_2^* and C orientations, and the resulting ODF becomes similar to the case for only slip (figure 5c, f, i).

As for only slip, the amount of C component in the VPSC simulations plus twinning can be varied by playing with the grain-shape updating (compare figure 5b, c with 5e, f). If the grain shape is not updated, a significant amount of A_1^* is retained at 2.5 strain. At 4.0 strain, the A_1^* are less intense but still practically no C is formed. On the contrary, if the grain shape is continuously updated, a high-SFE-like final texture with a strong C component is obtained once more. Finally, the FC model (completely insensitive to grain shape) gives an intermediate result (figure 5i): some A_1^* is retained but some C starts to reappear at the 4.0 strain.

5. Comparison of measured and simulated texture

(a) Medium-to-high SFE and/or high temperature

For high temperature or medium-to-high SFE, the major types of texture components that are observed in the experiments are those that are predicted in the simulations. However, the evolution of a preferred component or the relative proportions of components with increasing deformation are not simulated well. One exception is the better match between the VPSC model and the complete fibres observed in the higher temperature results (compare figure 2d, l with figure 4a, b). Generally, it is difficult to simulate the critical strain ranges for the appearance and disappearance of the C, A_1^* or A_2^* components, as well as their relative intensities, especially in the high-to-medium SFE materials at room temperature.

The simulations predict that the C, A_1^* or A_2^* components should rise and fall, as observed experimentally and best illustrated in the analytical model in Gilormini *et al.* (1990). While simulations predict a cyclic development, they do not predict the experimentally observed timing and the proportion of components in the cycle. Consider that the A_1^*, A_2^*, and C components lie along a special fibre defined by ⟨110⟩ along the radial direction. Analyses show that orientations can rotate along this fibre between the A_2^*, C and A_1^* components in a cyclical manner due to the magnitude of rigid-body spin about the radial direction (Toth *et al.* 1989; Gilormini *et al.* 1990). During this very long cycle, densities of crystallites build up and decay in a sequence of orientations from A_1^* to A_2^* to C to A_1^* and back. In the analytical calculations, the A_2^* component peaks in the first quarter of the cycle and then decays

to random by the middle of the cycle, at which point the C component has peaked. The length of this cycle period depends on the rate sensitivity m (i.e. $n = 1/m$). The period extends to infinity for rate-insensitive material and decreases to $\varepsilon_{vM} = 20$ for $m = 0.05$ (i.e. $n = 1/m = 20$) (Harren *et al.* 1989; Neale *et al.* 1990). Consequently, as shown in either the rate-sensitive Taylor FC or VPSC simulations in figure 4, a strong A_2^* still remains at $\varepsilon_{vM} = 4$. In contrast with the simulations, a rather short cycle is observed in the experiments at 296 K, with only a moderate build up of orientation densities around A_2^* occurring before a strain of $\varepsilon_{vM} = 1$ and decaying quickly to a level below random with increasing strain thereafter (figure 2*a*, *b*, *e*, *f*).

Similar shortened A_2^*, C cycles are observed experimentally in other FCC metals deformed in shear or by torsion, including aluminium (Montheillet *et al.* 1984; Rollett 1988), copper (Montheillet *et al.* 1984; Sekine *et al.* 1981; Stout *et al.* 1988; Stout & O'Rourke 1989; Williams 1962) and dilute copper–zinc alloys (Sekine *et al.* 1981). The initial texture can alter this result. For example, if the A_2^* component is fed with a favourable starting texture, as in a sample with common rolling texture with the prior rolling plane normal parallel to the shear direction, then the A_2^* intensity peaks earlier and at a higher intensity before decaying, as shown in the data of Williams (1962). Since the A_2^* peak in that case occurred at very low strains, $\varepsilon_{vM} = 0.2$, where textures are not usually measured, it could be easy to miss. Generally, A_2^* has been observed only as a very weak component in experiments because the texture is measured at larger strains, $\varepsilon_{vM} > 1.5$ (see, for example, Montheillet *et al.* 1984; Sekine *et al.* 1981; Stout *et al.* 1988; Stout & O'Rourke 1989). Rather than a strong A_2^* component, as suggested by the simulations, the C component is the strongest in both the current experiments for nickel and nickel–cobalt and in previous ones for moderate-to-high-SFE metals.

The C component in the experiments begins to dominate very early in the deformation as A_2^* disappears, $\varepsilon_{vM} = 2$, and strongly increases in intensity with increasing strain. In comparison, for a rate-sensitive material in the Taylor FC simulations, a dominant C component and the associated disappearance of A_2^* is only observed following extremely large strains $\varepsilon_{vM} > 5$. If relaxed constraints are used in the Taylor model, then the development of the A_2^* component is somewhat suppressed, while the C is increased, as shown first by Canova *et al.* (1984). Similarly, in the VPSC model, if the grain shape is evolved to match the geometry of the deformation, then A_2^* is decreased and the amount of C is enhanced at lower strains. Thus, the proportion of A_2^*, C and, to a lesser extent, A_1^* can be varied in the simulations by changing the rate sensitivity, the strain level and level of constraint based on the evolution of the grain shape.

However, even with these modifications and by using a higher rate sensitivity than observed experimentally, A_2^* is much too strong, while the relative proportion of C is too weak in simulations compared with experiment. This much shorter experimental cycle compared with prediction is related to the very flat shape of the dislocation microstructure and to grain subdivision. This microstructural contribution to the texture evolution will be discussed in the next sections.

The A and B components are also steady contributors to the experimental textures that are observed. However, their significance is lost in the Taylor simulations that predict the overriding dominance of A_2^*. The VPSC model does a better job of predicting the A and B components although the location of the 'B' texture peak in the VPSC model is displaced 15° from the ideal B along the ⟨110⟩ fibre.

(b) Low SFE and twinning

The low-SFE Ni + 60 wt% Co deformed at 296 K developed a significantly different texture than the high-SFE samples. The principal differences include the new texture components, $\{\bar{5}45\}\langle 652\rangle$, near the A_1^* component and the lack of a C component. Simulations, including this one, have been inspired by the early suggestions of Wasserman (1963) and Haessner & Kiel (1967), to introduce reorientation by twinning to effect the observed change in texture (Chin *et al.* 1969; van Houtte 1978). Later experimental studies in rolling have also lent support to this approach (Hu & Cline 1988; Donadille *et al.* 1989; Ray 1995) based on microstructural observations.

When twinning is added to the simulations, then reorientation of the texture occurs by both slip and twinning. Twinning in the simulations principally had one major change in the predicted texture, taking the strong A_2^* component formed by slip and reorienting it to the twin related A_1^* component. Thus, twinning occurred predominantly in one region of orientation space and along one twin system that was oriented to have the largest resolved shear stress with respect to the macroscopic applied stress. This change produces a texture similar to that observed in the experiments, in which a medium-strong partial fibre near A_1^* is observed (compare figures 2*j* and 5*e*). Note, however, that the experimental texture is characterized by new components 20° from A_1^*.

Reorientation by twinning also removed a small amount of the orientation density near the C component in the simulations, thereby lowering the amount of C that was formed. While some C is decreased in the simulations, it was difficult to eliminate the C in the simulations to a degree comparable with the experiment. In the VPSC model, this decrease in C was aided by not evolving the grain shape.

While several early investigators (e.g. Dillamore & Roberts 1965) have suggested that slip was more important to the texture change than twinning, only a couple of later investigators have been proponents of the contribution of slip. For example, Leffers & Bilde-Sørensen (1990), have suggested that the physical constraint of the twins on further slip in the matrix has a bigger effect on the texture development than the contribution from the actual crystal orientation of the twins. Duggan *et al.* (1978) also postulated that slip was more important than the small twin volume, based on their microstructural observations following rolling. The two more recent sets of investigators note that the rolling case is complicated by the early onset of twinning, and the microstructure and texture changes due to shear banding following twinning. Quantitative observations of the associated microstructure must be used to determine whether or not twinning is important and to what extent slip plays a role.

(c) Strength and intensity of the preferred texture

The simulations generally overpredict the degree of texture formation. The volume fractions and peak intensities in the experiments are, on average, 2–3 times less than those in the simulations. In the worst case at the largest strain, the Taylor FC model predicts a sharp peak for the A_2^* component that is 20 times that observed in the experiments. Generally, the VPSC model has lower peak intensities than the Taylor model and is, thus, a better match with experiment in this regard. Rather than having a sharp peak of intensity surrounding an ideal component, as in the

simulations, the experiments show a very broad distribution of moderate intensity about a preferred orientation (compare figure 2 with figure 4). The wide spread in orientations about an ideal component in the experiments, described by the half-width of the texture peak at half its maximum height, is twice that predicted by the VPSC and thrice that for the Taylor model. Note that much of the texture spread observed in the experiment lies outside of the regions counted in the volume fraction summation for the ideal components. A larger texture spread in experiments compared with the simulations is a common observation for many other deformation modes, including rolling (Hansen *et al.* 1993). One factor in this difference may be grain statistics in the simulations. As Matthies & Wagner (1996) have shown, the texture strength decreases for increasing numbers of individual orientations. Other explanations should be sought, such as grain subdivision by dislocation boundaries, since the difference is so large.

6. Microstructure

The microstructural aspects considered by the simulations were only the grain shape and deformation-induced twins. However, deformation creates a microstructure that includes volume elements surrounded by dislocation boundaries at a finer scale than a grain. These structures and the local orientation environment are considered next with respect to their impact on the observed macroscopic textures. The structural and orientation differences that occur as a function of temperature and SFE are highlighted.

The dislocation structures observed for the three materials and different deformation temperatures fit within the framework of grain subdivision by deformation-induced dislocation boundaries on two size-scales (Bay *et al.* 1992; Hansen & Hughes 1995). The smallest size-scale comprises equiaxed cells, while the larger scale comprises long, flat, geometrically necessary boundaries (GNBs) (Kuhlmann-Wilsdorf & Hansen 1991) that surround groups of cells arranged in long cell blocks (CBs). These GNBs include double-walled microbands (MBs), single dense dislocation walls (DDWs) and lamellar boundaries (LBs), which have been defined and described elsewhere (Bay *et al.* 1992). Microbands and DDWs are characteristic of the low-strain structures, $\varepsilon_{vM} \leqslant 0.8$, whereas the LBs are characteristic of the large-strain structures above $\varepsilon_{vM} = 1.9$. All types of GNBs may be observed at intermediate strains. The nearly parallel groups of GNBs that subdivide a grain are aligned macroscopically with respect to the torsion axis. At small strain, either one family or two intersecting families of MBs/DDWs are observed, with one family nearly parallel to the macroscopic shear plane (figure 7a) and the other at 60–90° to that plane (figure 7b). The number of subdividing GNBs within a grain increases from a few at very small strains, $\varepsilon_{vM} \leqslant 0.2$, to many at $\varepsilon_{vM} \geqslant 0.6$.

The aspect ratio of the cell blocks defined by the GNBs is not the same as the aspect ratio defined by the evolving grain shape. Optical metallography showed that the initially equiaxed grains elongated with increasing strain, as expected from geometrical considerations. As a result, the aspect ratio for grains changes very slightly from 1 at $\varepsilon_{vM} = 0$ to 1.01 at $\varepsilon_{vM} = 0.4$. In contrast with the whole grain, the aspect ratio of cell blocks defined by the GNBs ranges from 1 for grains with two families of intersecting GNBs, to roughly 3 in grains with one family of nearly parallel GNBs, even at a medium strain (compare parts (a) and (c) of figure 7). At large strains,
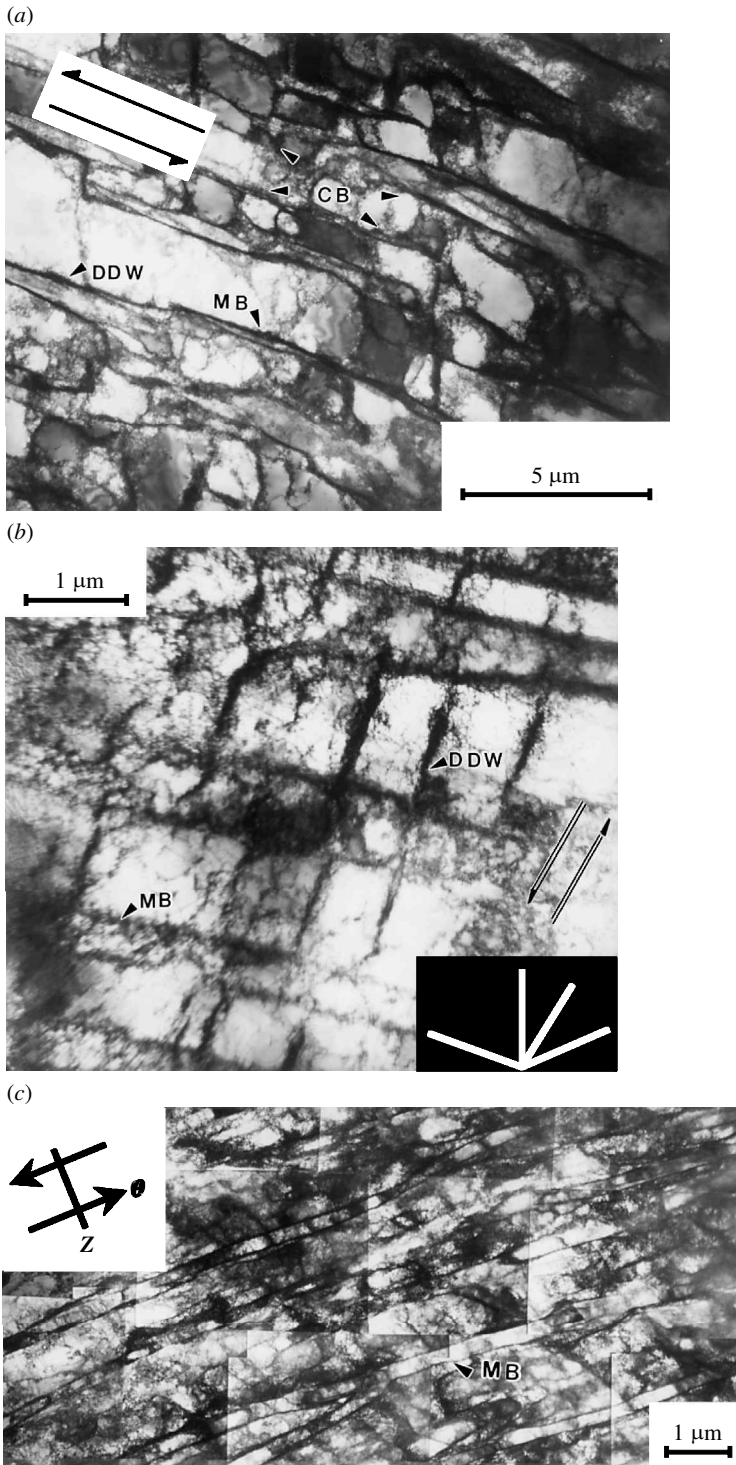
(a)

(b)

(c)

Figure 7. For description see opposite.

where $\varepsilon_{vM} \geqslant 1$, the structure is made up of closely spaced LBs nearly parallel to the shear plane (figures 7c and 8a–c). These flat LBs sandwich single layers of cells, forming cell blocks. This LB structure has a very high aspect ratio, ranging, approximately, from 3 to 5. Another common feature within the large-strain microstructure is groups of lenticular to nearly equiaxed subgrains that alternate with groups of LBs (figure 8b). The proportion of subgrains compared with LBs is much higher at the higher temperature of 573 K than at 296 K (compare parts (a) and (b) in figure 8).

While the framework of grain subdivision describes the general features of the microstructure for all of the materials, SFEs, temperatures and strain levels, these different conditions systematically influence the slip pattern and, thereby, the texture. For example, the spacing between all types of dislocation boundaries decreases with increasing strain, decreasing SFE and decreasing temperature. The misorientation angle across dislocation boundaries also increases with increasing strain. This increase occurs at a higher rate for the GNBs compared with the cell boundaries, resulting in the formation of high angle boundaries and a wide spread of different orientations within a single original grain. This result is shown in figure 9a, in which the minimum misorientation angle (disorientation) across dislocation boundaries in adjacent crystallites is plotted as a function of distance within a single grain. Many of the measured misorientation angles across the deformation-induced dislocation boundaries are very large and have angles characteristic of regular grain boundaries (see, for example, Hughes & Hansen 1997).

Note that the dislocation boundaries separate different texture components and that the grain has split up into many local orientations spread out widely along the various texture fibres. This result is superposed on the misorientation plot of figure 9a, in which the crystal orientation of adjacent crystallites is indicated by shading. An orientation type is assigned based on the criterion that the crystallite orientation is within $15°$ of an ideal texture component from table 2. Strikingly, nearly all of the ideal texture components are observed over a very short distance in one original grain. Similar behaviour is observed in Ni + 60 wt% Co (figure 9b), in which many orientations are observed over a short distance in two locations. The disorientations were measured mainly across adjacent dislocation boundaries. Only 10% of the boundaries measured were twin boundaries, as determined by their angle axis pair near $60° \langle 111 \rangle$. Note that these twin boundaries did not separate the A_1^* and A_2^* components, although the A_1^* was the predominant ideal orientation in both of these small regions. The A_1^* appeared to be part of the matrix material rather than the deformation twin.

Deformation twinning occurred as a deformation mechanism in conjunction with grain subdivision by dislocation boundaries depending on the SFE, strain level and temperature. Twinning was only observed in Ni + 60 wt% Co, i.e. the material with

Figure 7. TEM micrographs of the small-to-medium strain deformation microstructures showing that long dislocation boundaries form very early in the deformation. The shear directions are marked by double arrows. (a) Nickel deformed at 296 K, $\varepsilon_{vM} = 0.35$. This region is in a random orientation near $\{\bar{1}2\bar{1}\}\langle 41\bar{2}\rangle$ but within the texture spread about the B orientation. A cell block is marked CB; (b) Ni + 60 wt% Co deformed at 296 K, $\varepsilon_{vM} = 0.35$ showing two intersecting families of microbands (MBs) and DDWs that are nearly parallel to the {111} slip planes marked by four white lines in the bottom right-hand corner. (c) Ni + 30 wt% Co deformed at 296 K, $\varepsilon_{vM} = 1.2$. The MBs delineate lamellar regions along the shear plane.
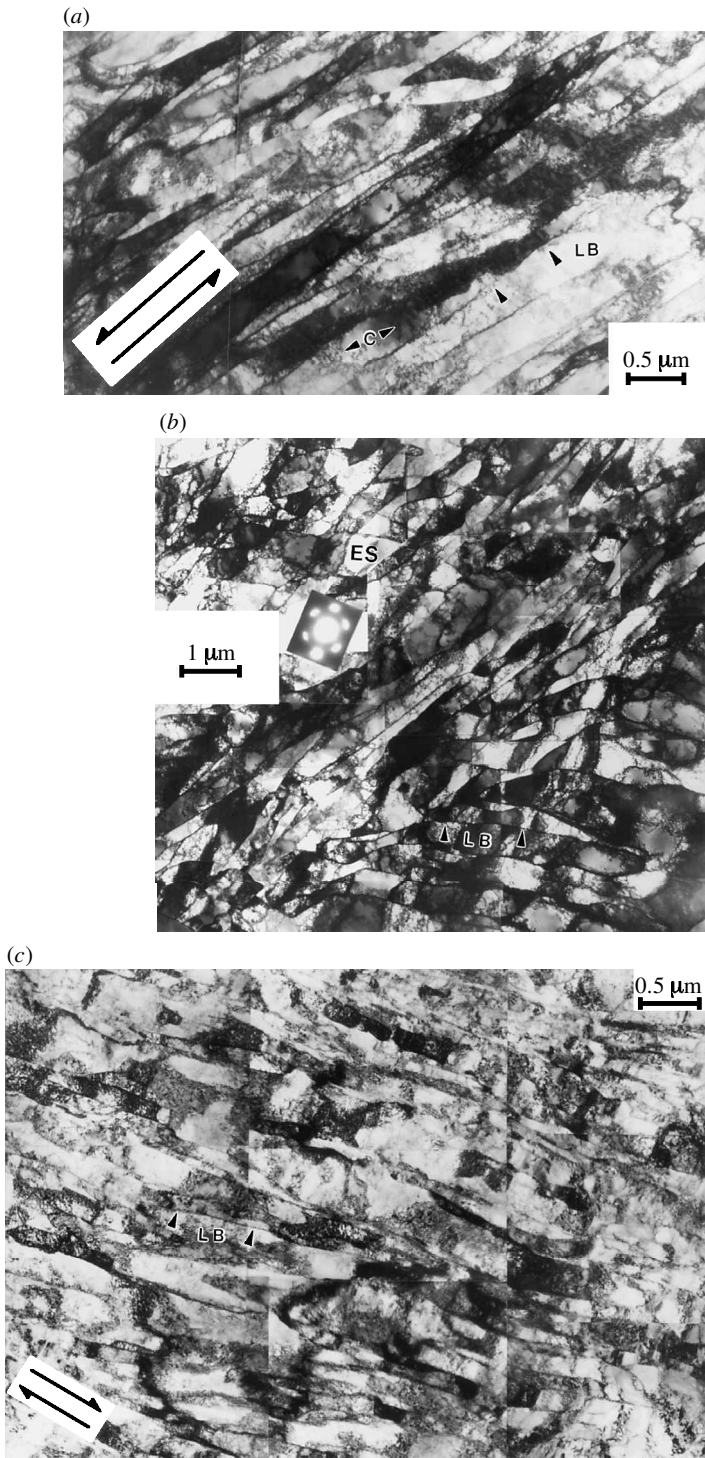
Figure 8. For description see opposite.

the lowest SFE. These observations based on TEM were corroborated with optical metallography. At medium strains, $\varepsilon_{vM} = 0.35$, and 296 K, there were a few isolated, very thin and small faulted regions observed in the TEM, which may have been incipient deformation twins. The deformation microstructure at $\varepsilon_{vM} = 0.35$, however, was dominated by the dislocation structure of intersecting MBs and DDWs. Following $\varepsilon_{vM} = 1$ at 296 K, a few very thin deformation twins were observed in isolated grains comprising less than a $\frac{1}{2}$ vol. % based on area measurements. As the strain increased to $\varepsilon_{vM} = 2$, many more thin deformation twins were observed on intersecting twin systems within the dislocation microstructure (figure 10a) but the actual volume fraction of these twins, $ca.\,5\%$, was still small.

These thin twins exhibited a wide variety of orientations and sizes. Frequently, the twins were oriented to cut across the lamellar cell blocks, effectively changing the aspect ratios of the lamellar cell blocks (figure 10b). These intersecting twins are macroscopically oriented at a high angle to the shear plane and are in contrast with other twins that lie in bundles roughly along the shear plane and parallel to the lamellar cell blocks. Twins were found in grains having a wide variety of crystal orientations, as well as in grains oriented near either A_1^* or A_2^*. The dominating dislocation microstructure had many short and thin, e.g. 10 nm wide, lamellae that could be mistaken morphologically for twins. However, measurements showed that the boundaries of these thin lamellae had only low-to-moderate misorientations, quite far from the high $60°/[111]$ misorientation angle/axis characteristic of twin boundaries. Overall, the GNBs Ni + 60 wt% Co defined more fragmented and square-shaped cell blocks compared with the lamellar cell blocks observed at similar strains in the materials with the higher SFE (compare parts (a) and (c) of figure 7, and also figure 8a with figure 10a). As another difference, the cell boundaries were ill-defined, and some uniform distributions of dislocations in Taylor lattices were observed.

In contrast with the observations at 296 K, deformation twins still comprised less than $\frac{1}{2}$ vol. % following deformation at 573 K, and the largest strain of $\varepsilon_{vM} = 2.2$ (figure 8c). The dislocation structures including cells were more refined than at the lower temperature. While many square-shaped cell blocks were still observed, the proportion of lamellar cell blocks increased significantly. Thus, the overall microstructure was intermediate between the low-SFE low-temperature and the high-SFE low-temperature microstructures.

7. Relation between texture and microstructure

A variety of both textures and microstructures has been shown as functions of SFE, material, temperature and strain in the preceding sections. When these textures and microstructures are plotted together, as in figure 11, then it is observed that conditions leading to similar textures also lead to similar microstructures. This remarkable commonality will be discussed below using some instructive insight from the simulations. What is important to note is that differences in the dislocation slip pattern alone, without crystal reorientation by twinning, cause dramatic changes in the

Figure 8. TEM micrographs of the large strain dislocation structure composed of lamellar dislocation boundaries sandwiching thin layers of cells (C). (a) Nickel deformed at 296 K, $\varepsilon_{vM} = 2.1$; (b) nickel deformed at 573 K, $\varepsilon_{vM} = 2.1$; (c) Ni + 60 wt% Co deformed at 573 K, $\varepsilon_{vM} = 2.2$, showing a region with local orientations along the $\langle 110 \rangle$ fibre between the A and B ideal components.
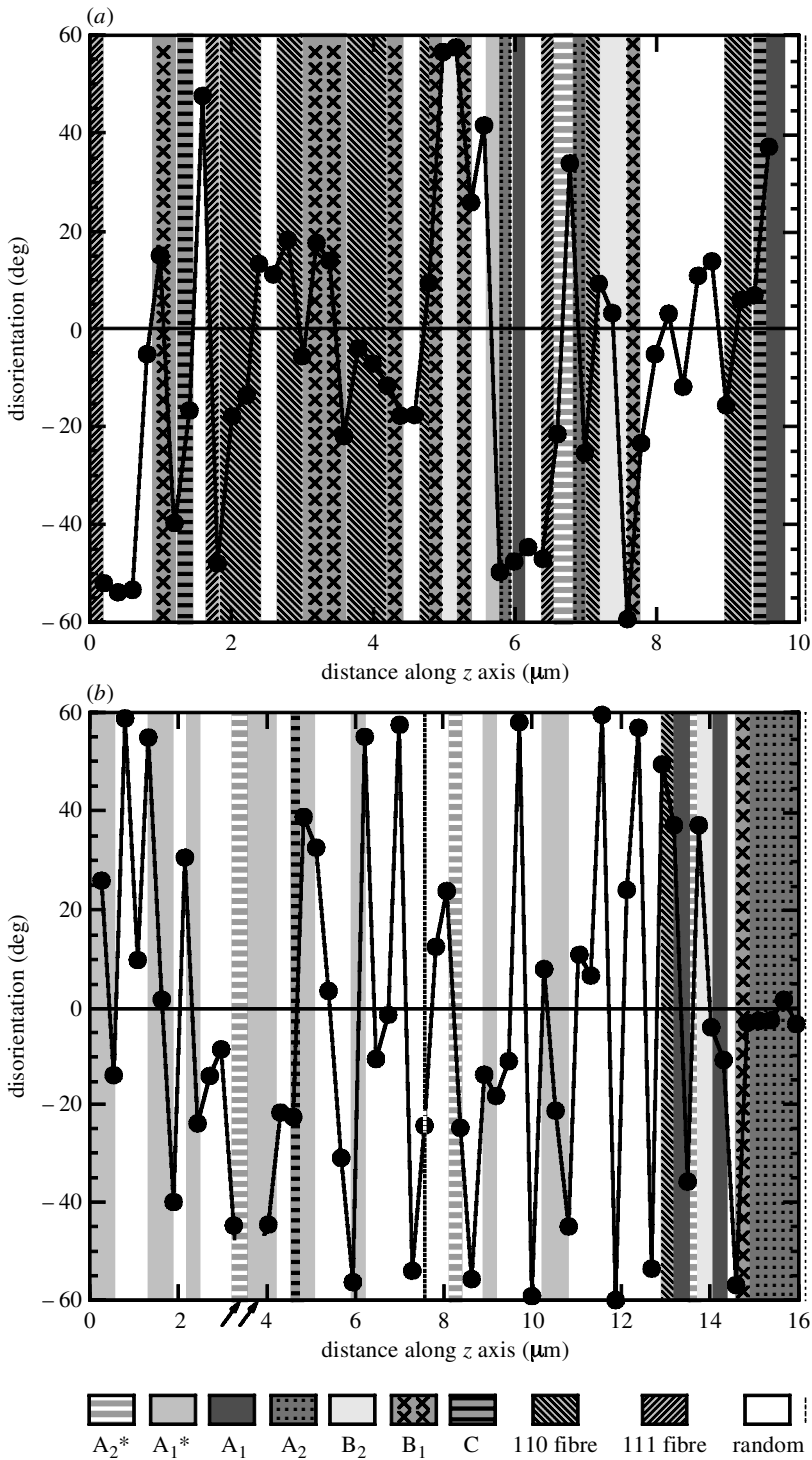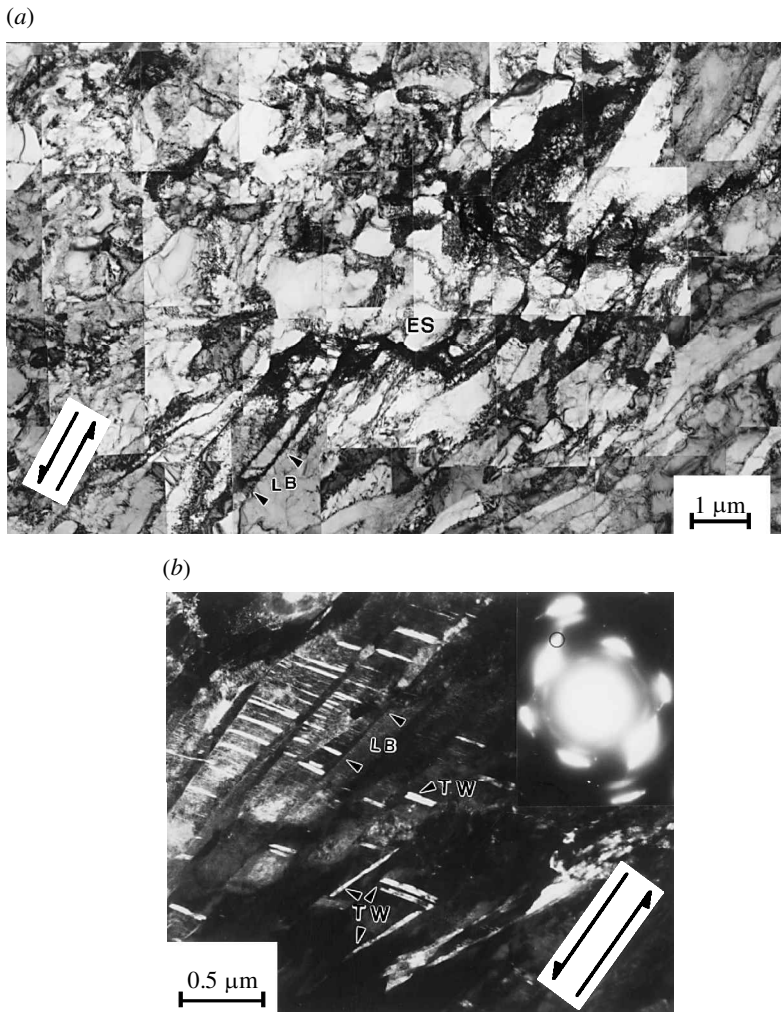
Figure 9. For description see opposite.

(*a*)

(*b*)

Figure 10. TEM micrographs of deformation microstructures that develop in the low-SFE Ni + 60 wt% Co at 296K. (*a*) Dislocation structure composed of LBs and equiaxed subgrains (ESs); there are no deformation twins in this region, $\varepsilon_{vM} = 1.2$; (*b*) TEM dark field micrograph showing 'white' deformation twins (TWs) cutting across lamellar bands, $\varepsilon_{vM} = 2.1$.

observed texture. The different orientations that develop within a grain demonstrate the influence of the local slip pattern (figure 9). Because the slip pattern is important to the texture evolution, the temperature and SFE, which affect slip, are thereby also very important.

Figure 9. The disorientation angles measured across adjacent dislocation boundaries in the axial direction, z, for torsion show an alternating character with distance. These boundaries separate finely distributed texture components, as shown by the shading. (*a*) Nickel deformed at 296 K, $\varepsilon_{vM} = 4.0$; (*b*) Ni + 60 wt% Co deformed at 296K, $\varepsilon_{vM} = 1.2$. Two separate regions in the sample were measured as marked by the arrows.
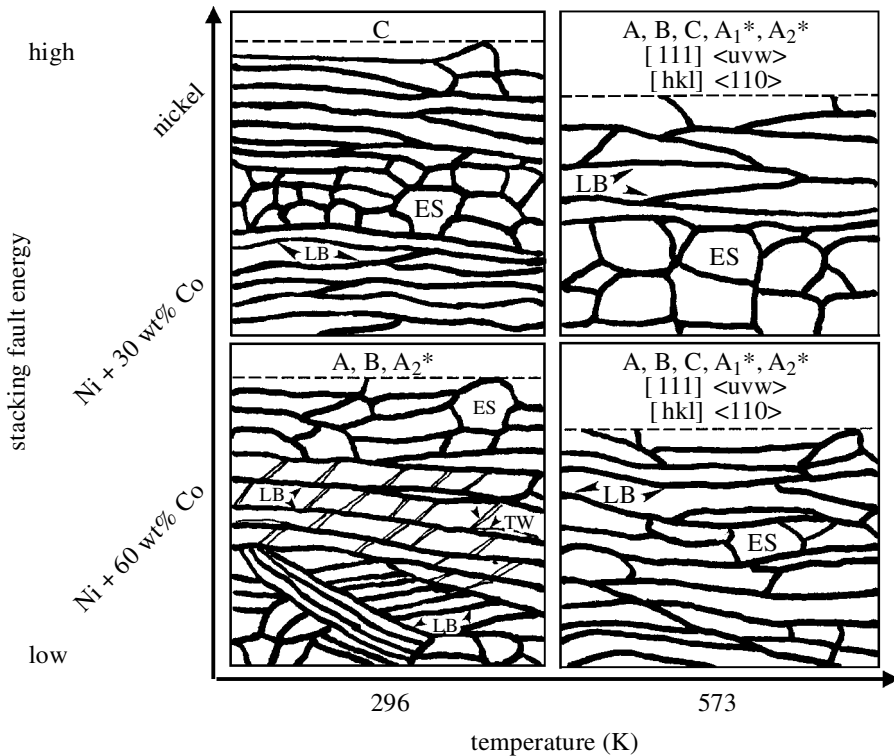
Figure 11. Schematic showing the major characteristics of the three types of textures and microstructures that develop at large strain as a function of material, SFE and temperature. Only the GNBs are shown in the schematic. LB indicates lamellar dislocation boundaries. ES indicates equiaxed subgrains. TW indicates short thin deformation twins that either cut across the lamellar bands or lie along the lamellar boundaries.

(a) Slip or twinning?

The microstructure and texture observations show that the distinctive low-SFE and low-temperature texture (figure 2i) was formed *before* the onset of twinning. In the absence of twinning, the microstructure and textures are controlled by dislocation slip and the ease with which dislocations cross-slip. High SFE and temperature encourage cross-slip. Thus, although twinning in the simulation appeared to give the correct texture, it is not the principal mechanism that is active in the experiments, as revealed by the microstructural observations. Secondly, the twinning was only observed following large strain in the experiment. These twins were not just along one or two systems in special grain orientations, but occurred in a wide variety of grain orientations and along 2–3 twin systems per grain. Most twin systems were not the twin system with the highest resolved shear stress based on the macroscopic applied stress state. The variety of systems observed is explained by the fact that deformation twins have a threshold stress for initiation of a twin. Therefore, twin formation is linked to the very local stress state at the level of the dislocation boundary. Thus twin systems can be activated by local stresses that are different from the ones predicted by the applied macroscopic or even grain-level stresses.

Consequently, only in a few very special cases do the observed twins reorient material to a main texture component. Thus, most of the twins reorient the twinned material to locations in orientation space that are away from the main texture components, thereby adding to the random level. Of course, some twins of A_1^* orientation do form in the experiments in both A_2^* oriented grains and in grains near C, as predicted, but the twin volume fraction is far too small to make up the strong intensity of orientations near A_1^* that are observed in the experimental ODFs.

Grains near the A_1^* component arise by slip mechanisms as well as by twinning. This possibility is demonstrated by both the experiment and the VPSC simulation without twinning. The A_1^* component was observed for experimental textures developed at 573 K without twinning (figure 2d, nickel) or with very little twinning (figure 2l, Ni + 60 wt% Co). Several A_1^* oriented crystallites that were not deformation twins—as determined by their size, shape, and boundary character—were also observed in the TEM for Ni + 60 wt% Co deformed at 296 K (e.g. figure 9b). The VPSC simulation for only slip also predicts a moderate A_1^* component at low-to-medium strains. Thus, the A_1^* component observed in the low-SFE texture at 296 K arises mostly from slip, with twinning making up a smaller fraction at the very largest strains.

Neither the new texture components nor the low value for the A_2^* in the low-SFE low-temperature experiment is explained by the microstructural results discussed thus far. It may be that texture development is more retarded in the low-SFE metal so that the texture never develops much beyond the formation of the initial A_1^* component suggested by the analysis of Gilormini *et al.* (1990). The more complete answer must, however, be found in the development of the slip pattern within grains as a function of SFE and temperature.

(*b*) *Slip patterns revealed by grain subdivision*

Geometrically necessary dislocation boundaries subdivide a grain into differently deforming regions that slip with fewer slip systems than the number required by a Taylor analysis (Kuhlmann-Wilsdorf & Hansen 1991; Bay *et al.* 1992). These regions therefore act collectively to accommodate the deformation on average. Neighbouring regions deform with either different selections of slip systems, different partitions of slip on the same slip systems, and/or different amounts of strain. These GNBs accommodate the lattice mismatch that develops as a consequence of the slip selection.

This selection and partitioning of slip systems within cell blocks will be influenced by the SFE and the temperature. Low SFE and low temperature restrict dislocation mobility and thus promote planar glide. As the SFE and/or temperature is/are increased, thermally activated cross-slip of dislocations is easier, thus reducing the tendency for planar glide. More slip systems would also be active. Thus, the choice and number of slip systems in cell blocks for a low-SFE metal will be biased by the material's tendency for planar slip. This bias would differ from that of high-SFE materials.

Differences in local slip system selections in the cell blocks will result in differences in local lattice rotations as a function of SFE. Thus, it is postulated that some grains in a low-SFE metal favouring planar glide, like Ni + 60 wt% Co deformed at 296 K, will subdivide along different fibre textures than a high-SFE material such as pure nickel. This view is supported by the local orientation data in figure 9, which show

that one grain in Ni + 60 wt% Co has broken into the distinctive fibre texture from B_2 to A_2. As temperature is increased, the bias towards planar slip is reduced and the microstructure and texture evolution approach that of the high-SFE metal.

Note that this postulate regarding planar slip is new because it considers planar slip within the context of grain subdivision into differently deforming regions. The association of grain subdivision into different regions of planar slip is distinct from the lower bounds or Sachs-type hypothesis applied to a grain as a whole.

The local lattice rotations will reflect not only the slip system activity caused by the applied deformation but also slip activity caused by the presence of the dislocation boundaries (and deformation twins). These different sources of slip-system activity will further modify the texture development.

(c) Cell-block shape as a result of grain subdivision and twinning

The simulations showed that subtle changes to the texture can be made by incorporating differing deformation constraints due to the crystal shape. Both grain subdivision and deformation twinning create new volumes in cell blocks within a grain. The cell-block shape as a function of SFE and temperature correlates with the observed changes in the texture. The evolving cell-block shapes differ from the evolving grain shape (see figures 7 and 8). Crystal or grain shape influences the progression of orientations along the A_1^*, A_2^* to C radial fibre, as shown by the simulations. While an evolving grain shape was applied in the simulations at the level of the original grains for illustration, in the future, these constraints need to be applied with respect to the shape evolution of the deformation microstructure.

For the case of medium-to-high-SFE materials at 296 K, the early development of lamellar-shaped cell blocks (figure 7a) in the shear direction correlates with a strongly enhanced evolution of the C component relative to the other texture components along the $\langle 110 \rangle$ and $\{111\}$ fibres. At the same time, lamellar cell blocks disfavour the weakly observed A_2^* component. This strong enhancement of C decreases with increasing temperature as relatively larger proportions of more equiaxed subgrains are formed in combination with the lamellar substructure. Consequently, more uniform and complete $\{111\}$ and $\langle 110 \rangle$ fibre textures are observed at the higher temperature of 573 K. The low-SFE Ni + 60 wt% Co has a mixed equiaxed and lamellar microstructure like nickel at this higher temperature, as well as a similar fibre texture.

For the low-SFE material at 296 K, the dislocation structure generally tends towards more equal sided blocks and is not as well defined as that for the high-SFE material over the entire strain range. The deformation constraints required by the more equal sided structure suppress the formation of the C component, which would be favoured for flat shapes along the shear direction. At larger strains, regions with cell blocks formed by lamellar boundaries also contain a small volume fraction of twins. This twinning occurs on several twin systems that cut across the lamellar cell blocks creating square rather than lamellar-shaped volumes (see schematic in figure 11). Thus, the texture is affected by how the twins change the shape of the cell block, rather than by the crystal orientation of the twin. Consequently, in the simulations, a better match with the experiment is found if the grain shape is artificially limited in its evolution when twinning starts (compare parts (e) and (b) of figure 5), thereby suppressing the C component as in the low-SFE Ni + 60 wt% Co at 296 K.

8. Summary and conclusions

The different slip patterns formed within a single grain are at odds with the central Taylor assumption. How well the Taylor assumption is fulfilled on average depends on the SFE and deformation temperature, as is clearly shown by the development of new texture components. The wide variety of textures and microstructures observed as a function of SFE and temperature was developed by slip processes alone. It is hypothesized that the low-SFE slip pattern is a cause of the observed new texture components, which are distinct from the generally accepted ideal components obtained by modelling. These discrepancies are related to the microstructure effects determined by the slip pattern. Materials and conditions with similar deformation microstructures developed similar textures in the experiments, regardless of the SFE. Some deformation twins formed in the low-SFE material, but only at large strains after the texture was formed by slip. Upon further evolution at large strain, this twinning did not alter the distinctive character of the low-SFE texture formed originally by slip.

The most important mechanism that creates the new texture components is the local slip pattern, reflected in the grain subdivision into cell blocks. The slip-system selection and partitioning, creating the different lattice rotations within a cell block, is altered by the planarity of slip. Slip planarity is controlled by the SFE and temperature. Thus, some grains in low-SFE metals deformed at low temperature will subdivide along different fibre textures than those in high-SFE metals, as shown by detailed measurements of the microstructure. Additionally, new slip systems are activated as a result of the grain subdivision that are not included in the texture models. In the future, detailed analyses of the dislocations that compose the GNBs surrounding cell blocks will provide additional keys to these slip-pattern differences. Future refinements of polycrystal plasticity simulations will need to include the characteristics of the microstructure. Clearly, a grain cannot be considered as a homogeneous unit in realistic models of the deformation process.

More subtle effects of microstructure on the texture arise from the different deformation constraints allowed by different shaped cell blocks. Grain subdivision by dislocation boundaries in these materials created different cell-block shapes that correlated with the different textures observed as a function of SFE and temperature. The evolution of the cell-block shapes within the grains differs from the grain-shape evolution. These different shapes correlated with the presence or absence of certain ideal texture components whose evolution could not be simulated.

Appendix A.

A brief overview of the simulation methods, including a description of how twinning is implemented in the model, is given in this appendix. Detailed accounts of the VPSC simulation methods used herein have been published before. For readers wanting more detail, the development of the VPSC model can be traced in terms of the Eshelby (1957) inclusion formalism by Hill (1965) and Hutchinson (1970, 1976), and
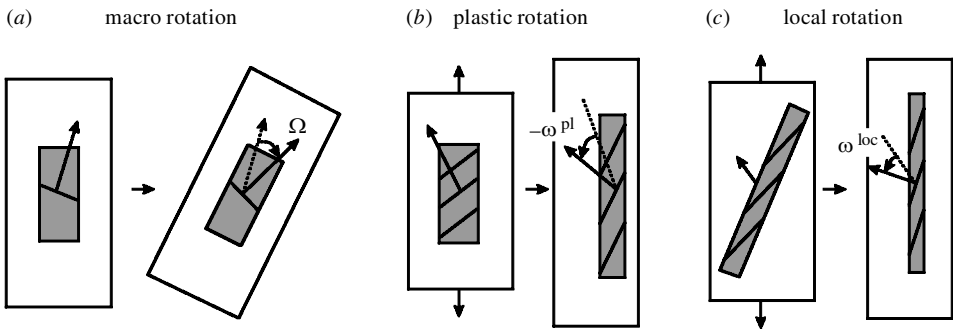
Figure 12. Schematic of the three rotation terms in equation (A 1).

the general *n*-site approach for large-strain viscoplasticity of Molinari *et al.* (1987), leading to the 1-site approximation by Lebensohn & Tomé (1993). For both Taylor and VPSC, the viscoplastic approach is used at the single-crystal level. Thus, if a strain-rate is applied to a single crystal (grain) and the geometry and critical stresses of the active slip and twinning systems are known, the stress in the grain can be calculated by solving a system of nonlinear equations. In the FC case, whereas the local strain rates in all grains are assumed to be equal to the macroscopic applied strain rate, the local stresses can be readily calculated and the macro stress obtained as an average of those local stresses.

   Unlike the FC approach, within the VPSC formulation, the stress and strain rate in the grains can be different from the corresponding macroscopic magnitudes. The deviations of the local magnitudes with respect to the macroscopic ones depend on the directional plastic properties of the grains and the whole polycrystal. Basically, the VPSC model regards each grain of the polycrystal as a viscoplastic inclusion deforming in a viscoplastic homogeneous effective medium (HEM), having the average properties of the polycrystal. The VPSC formulation is based on the determination of the interaction tensor that relates the local deviations in stress and strain rate with respect to the macroscopic state. The interaction tensor depends on the viscoplastic Eshelby tensor (which, in turn, depends on the grain shape) and on the macroscopic modulus. The latter is not known *a priori*, but can be determined self-consistently by imposing the conditions that the averages of the local stresses and strain rates over all of the grains should match with the corresponding applied macroscopic magnitudes. Consequently, the influence of grain morphology enters more gradually in the VPSC approach (Tiem *et al.* 1986), compared with the complete relaxation of some components of the strain as a consequence of the grain morphology assumed by the Taylor RC theory (Honneff & Mecking 1981; Canova *et al.* 1984).

   The total deformation is applied to the polycrystal as a sequence of incremental deformation steps. After each step, the grain shape, the texture and the critical stresses are updated due to stretching, grain rotation and strain hardening, respectively.

(*a*) *Grain rotations by slip and twinning*

   In order to predict texture development, it is necessary to determine the rotations of the grains. When slip is the only operative mechanism of plastic deformation, the

total rotation rate of a grain is given by

$$\dot{\omega} = \dot{\Omega} - \dot{\omega}^{\mathrm{pl}} + \dot{\omega}^{\mathrm{loc}}, \tag{A 1}$$

where the terms on the right-hand side are the macro, plastic and local rotation rates, respectively. The first term (macro) is related to the rotation of the sample during a torsion test. The second one (plastic) can be readily derived from the shear rates. The third term (local) depends on the magnitude of the local deviations in strain and on the assumed grain shape, and it is zero in the FC case. On the other hand, in the VPSC case, the local rotation rate can obtained as

$$\dot{\omega}^{\mathrm{loc}} = \tilde{\dot{\omega}} = \boldsymbol{\Pi} : \boldsymbol{S}^{-1} : \tilde{\dot{\varepsilon}}, \tag{A 2}$$

where $\boldsymbol{S}$ and $\boldsymbol{\Pi}$ are the symmetric and skewsymmetric (Lebensohn & Tomé 1993) viscoplastic Eshelby tensors, respectively, and $\tilde{\dot{\varepsilon}} = \dot{\varepsilon} - \dot{E}$ and $\dot{\boldsymbol{E}}$ are the macroscopic and local strain rates, respectively. Particularly, the $\boldsymbol{\Pi}$ tensor vanishes for spherical grains, while its norm increases—and so does the weight of $\dot{\omega}^{\mathrm{loc}}$ in expression (A 2)— as the grain shape becomes more severely elongated.

Figure 12 clarifies the meaning of the three rotation terms in equation (A 1). When a polycrystal undergoes a rigid-body (macro) rotation (figure 12a), each grain in the polycrystal rotates by the same amount. If the polycrystal deforms plastically and so does a grain inside, the slip activity involves a rotation of the crystal lattice due to the constraints that the polycrystal as a whole exerts on the grain. Figure 12b shows a simple example of a polycrystal undergoing uniaxial tension with an embedded grain whose lattice rotates while the grain deforms plastically by slip. Finally, if a non-equiaxed grain deforms differently from the polycrystal, the local rotation tends to align the principal directions of the grain and the strain path applied to the polycrystal. Figure 12c shows the extreme case of a highly elongated, non-deforming grain embedded in a polycrystal deforming under uniaxial tension. In this case, the long direction of the grain tends to align with the tensile direction.

An additional source of rotations is related to twinning activity. When a twin is formed inside a given crystal, some volume fraction of it adopts a completely different but crystallographically related orientation. Several schemes have been proposed (Tomé *et al.* 1991; Lebensohn & Tomé 1993; van Houtte 1978) to deal with the effect of twinning reorientation in texture development. Particularly, for moderate twinning activities (i.e. when slip participates more than twinning in plastic strain accommodation, as in FCC materials), the so-called predominant twin reorientation (PTR) scheme (Tomé *et al.* 1991) has been shown to be good enough to capture the main role of twinning reorientation in texture development. Briefly, the PTR scheme consists of the following steps.

(1) Keep track of three magnitudes associated with twinning: namely (a) $F^{\mathrm{g,s}}$, the volume fraction of each twin system (s) inside each grain (g), given by the accumulated shear associated with that twin divided by the characteristic twin shear; (b) F^{tot}, the sum of the individual $F^{\mathrm{g,s}}$ over all systems and grains; and (c) F^{eff}, the effective twinned fraction reoriented according to the random selection described below.

(2) If F^{eff} is less than F^{tot}, make a random choice of a grain (g) and perform a complete reorientation of that grain to the orientation associated with the twin

system (s) if

$$F^{\mathrm{g,s}} > 0.25 + 0.25 \times \frac{F^{\mathrm{eff}}}{F^{\mathrm{tot}}}. \tag{A 3}$$

In this way, reorientation by twinning takes place in those twin systems that exhibit the highest activity in the grain throughout the deformation process. Furthermore, as the actual twinned fraction, F^{tot}, grows larger than the effective twinned fraction F^{eff}, the second term of the sum in the right-hand side decreases and further reorientation by twinning is favoured until F^{eff} 'catches up'. Such a procedure is self-correcting and both fractions tend to remain approximately equal throughout deformation. When both fractions are equal, condition (A 3) will be fulfilled if the volume of the twin represents more than half of the total volume of the grain. If this is the case, the whole grain will adopt the orientation of that 'predominant' twin. The two values 0.25 in equation (A 3) are rather arbitrary, but the choice of any other pair of positive numbers that sum to 0.5 does not significantly change the results.

(b) Hardening law

Texture development predictions of single-phase materials do not depend, in practice, on the actual value of the macroscopic stress applied to the polycrystal or on the absolute values of the critical stresses, but only on their relative values. Thus, the known changes in hardening as a function of temperature would not change the texture results in these simulations. Since we are only interested in texture, the temperature effect on hardening was neglected. Deformation temperature was only considered implicitly as a factor in determining when twinning was active in the simulation. Furthermore, when both slip and twinning were assumed to be active, we adopted a simple linear hardening law, given by

$$\Delta\tau_{\mathrm{c}}^{\mathrm{sl}} = h^{\mathrm{sl}}\Delta\Gamma, \qquad \Delta\tau_{\mathrm{c}}^{\mathrm{tw}} = h^{\mathrm{tw}}\Delta\Gamma, \tag{A 4}$$

where $\Delta\tau_{\mathrm{c}}^{\mathrm{sl}}$ and $\Delta\tau_{\mathrm{c}}^{\mathrm{tw}}$ are the increments in the critical stresses of every slip and twinning system, respectively, $\Delta\Gamma$ is the increment of the total shear in the grain (i.e. the sum of shears in every slip and twinning systems), and h^{sl} and h^{tw} are two independent hardening parameters for slip and twinning, respectively. In the slip plus twinning simulation that follows, we adopted h^{sl} equal to zero and h^{tw} equal to a given positive value. In this way, we prevented an unbounded increase of the twinned volume fraction, keeping it in a good agreement with the experimental evidence. On the other hand, when only slip was considered as the active deformation mechanism, the critical stress of slip was assumed to be constant along the calculation.

References

Bay, B., Hansen, N., Hughes, D. A. & Kuhlmann-Wilsdorf, D. 1992 Evolution of FCC deformation structures in polyslip. *Acta Metall. Mater.* **40**, 205–219.

Beaudoin, A. J., Dawson, P. R., Mathur, K. K. & Kocks, U. F. 1995 A hybrid finite-element formulation for polycrystal plasticity with consideration of macrostructural and microstructural linking. *Int. J. Plast.* **11**, 501–521.

Beaudoin, A. J., Mecking, H. & Kocks, U. F. 1996 Development of local orientation gradients in FCC polycrystals. *Phil. Mag.* **73**, 1503–1517.

Becker, R. 1991 Analysis of texture evolution in channel die compression—effects of grain interaction. *Acta Metall.* **39**, 1211–1230.

Becker, R. 1995 A material size scale through crystal boundary energy. *Mod. Sim. Mater. Sci. Engng* **3**, 417–435.

Becker, R. & Panchanadeeswaran, S. 1989 Crystal rotations represented as Rodrigues vectors. *Text. Microstruct.* **10**, 167–194.

Beeston, B. E. P., Dillamore, I. L. & Smallman, R. E. 1968 The stacking fault energy of some nickel cobalt alloys. *Metal. Sci. J.* **2**, 12–14.

Bronkhorst, C. A., Kalidindi, S. R. & Anand, L. 1992 Polycrystalline plasticity and the evolution of crystallographic texture in FCC metals. *Phil. Trans. R. Soc. Lond.* A **341**, 443–477.

Butler, G. C., Graham, S., McDowell, D. L., Stock, S. R. & Ferney, V. C. 1998 Application of the Taylor polycrystal plasticity model to complex deformation problems. *J. Engng Mater. Tech. Trans. ASME* **120**, 197–205.

Canova, G. R., Kocks, U. F. & Jonas, J. J. 1984 Theory of torsion texture development. *Acta Metall.* **32**, 211–226.

Canova, G. R., Wenk, H. R. & Molinari, A. 1992 Deformation modeling of multiphase polycrystals: case of a quartz mica aggregate. *Acta. Metall. Mater.* **40**, 1519–1530.

Chin, G. Y., Hosford, W. F. & Mendorf, D. R. 1969 Accommodation of constrained deformation in f.c.c. metals by slip and twinning. *Proc. R. Soc. Lond.* A **309**, 433–456.

Dillamore, I. L. & Roberts, W. T. 1965 Preferred orientation in wrought and annealed metals. *Metall. Rev.* **10**, 271–380.

Donadille, C., Valle, R., Dervin, P. & Penelle, R. 1989 Development of texture and microstructure during cold-rolling and annealing of FCC alloys: example of an austenitic stainless steel. *Acta Metall.* **37**, 1547–1571.

Duggan, B. J., Hatherly, M., Hutchinson, W. B. & Wakefield, P. T. 1978 Deformation structures and textures in cold-rolled 70:30 brass. *Metal Sci.* **12**, 343–351.

Eshelby, J. D. 1957 The determination of the elastic field of an ellipsoidal inclusion and related problems. *Proc. R. Soc. Lond.* A **451**, 376–396.

Frank, F. C. 1988 Orientation mapping. In *Proc. 8th Int. Conf. Textures of Materials* (ed. J. S. Kallend & G. Gottstein), pp. 3–13. Warrendale, PA: The Metallurgical Society.

Gil Sevillano, J., van Houtte, P. & Aernoudt, E. 1980 Large strain work hardening and textures. *Prog. Mater. Sci.* **25**, 69–412.

Gilormini, P., Toth, L. S. & Jonas, J. J. 1990 An analytical method for the prediction of ODFs with application to the shear of FCC polycrystals. *Proc. R. Soc. Lond.* A **430**, 489–507.

Haessner, F. & Kiel, D. 1967 Orientierungsverteilung der kristallite in gewalztem Ms 70, bestimmt mit Hilfte elektronenmikroskopischer feinbereichsbeugung. *Z. Metallk.* **58**, 220–227.

Hansen, N. & Hughes, D. A. 1995 Analysis of large dislocation populations in deformed metals. *Physica Status Solidi* (b) **149**, 155–172.

Hansen, N., Juul Jensen, D. & Hughes, D. A. 1993 Textural and microstructural evolution during cold-rolling of pure nickel. In *Proc. 10th Int. Conf. Textures of Materials (ICOTOM 10)* (ed. H. J. Bunge), pp. 693–700. Clausthal: Trans Tech.

Harren, S., Lowe, T., Asaro, R. & Needleman, A. (eds) 1989 Analysis of large-strain shear in rate-dependent face-centred cubic polycrystals: correlation of micro- and macromechanics. *Phil. Trans. R. Soc. Lond.* A **328**, 443–500.

Hecker, S. S. & Stout, M. G. 1982 Strain hardening of heavily cold worked metals. In *Deformation processing and structure* (ed. G. Krauss), pp. 1–46. Metals Park, OH: ASM.

Hill, R. 1965 Continuum micromechanics of elasto-plastic polycrystals. *J. Mech. Phys. Solids* **13**, 89–101.

Honneff, H. & Mecking, H. 1981 In *Proc. 6th Int. Conf. Textures of Materials (ICOTOM 6)* (ed. S. Nakashima), pp. 347–355. Tokyo: The Iron and Steel Institute of Japan.

Hu, H. & Cline, R. S. 1988 On the transition mechanism of texture transition in face centered cubic metals. *Text. Microstruct.* **8–9**, 191–206.

Hughes, D. A. & Hansen, N. 1997 High angle boundaries formed by grain subdivision mechanisms. *Acta Mater.* **45**, 3871–3886.

Hughes, D. A. & Nix, W. D. 1988 The absence of steady-state flow during large strain deformation of some FCC metals at low and intermediate temperatures. *Metall. Trans.* A **19**, 3013–3024.

Hughes, D. A. & Nix, W. D. 1989 Strain hardening and substructural evolution in Ni–Co solid solutions at large strains. *Mater. Sci. Engng* A **122**, 153–172.

Hutchinson, J. W. 1970 Elastic-plastic behavior of polycrystalline metals and composites. *Proc. R. Soc. Lond.* A **319**, 247–272.

Hutchinson, J. W. 1976 Bounds and self-consistent estimates of creep of polycrystalline materials. *Proc. R. Soc. Lond.* A **348**, 101–127.

Kocks, U. F., Tomé, C. N. & Wenk, H. R. 1998 *Texture anisotropy: preferred orientations in polycrystals and their effects on material properties*. Cambridge University Press.

Kuhlmann-Wilsdorf, D. & Hansen, N. 1991 Geometrically necessary, incidental and subgrain boundaries. *Scripta Metall. Mater.* **25**, 1557–1562.

Kumar, A. & Dawson, P. R. 1995 Polycrystal plasticity modeling of bulk forming with finite elements over orientation space. *Comp. Mech.* **17**, 10–25.

Lebensohn, R. A. & Tomé, C. N. 1993 A self-consistent anisotropic approach for the simulation of plastic deformation and texture development of polycrystals—application to zirconium alloys. *Acta Metall. Mater.* **41**, 2611–2624.

Leffers, T. & Bilde-Sørensen, J. B. 1990 Intra- and intergranular heterogeneities in the plastic deformation of brass during rolling. *Acta Metall. Mater.* **38**, 1917–1926.

Liu, Q. 1994 A simple method for determining orientation and misorientation of the cubic crystal specimen. *J. Appl. Cryst.* **27**, 755–761.

Matthies, S. & Wagner, F. 1996 On a $1/n$ law in texture related single orientation analysis. *Physica Status Solidi* (b) **196**, K11–K15.

Molinari, A., Canova, G. R. & Ahzi, S. 1987 A self consistent approach of the large deformation polycrystal viscoplasticity. *Acta Metall.* **35**, 2983–2994.

Montheillet, F., Cohen, M. & Jonas, J. J. 1984 Axial stresses and texture development during the torsion testing of Al, Cu and α-Fe. *Acta Metall.* **32**, 2077–2089.

Neale, K. W., Toth, L. S. & Jonas, J. J. 1990 Large strain shear and torsion of rate-sensitive FCC polycrystals. *Int. J. Plast.* **6**, 45–61.

Ray, R. K. 1995 Rolling textures of pure nickel, nickel–iron and nickel–cobalt alloys. *Acta Metall. Mater.* **43**, 3861–3872.

Rollett, A. D. 1988 Strain hardening at large strains in aluminum alloys. PhD thesis, Drexel University.

Sekine, K., van Houtte, P., Gil Sevillano, J. & Aernoudt, E. 1981 The transition of torsional deformation textures in FCC metals. In *Proc. 6th Int. Conf. Textures and Materials (ICO-TOM 6)* (ed. S. Nagashima), pp. 396–407. Tokyo: The Iron and Steel Institute of Japan.

Stout, M. G. & O'Rourke, J. A. 1989 Experimental deformation textures of OFE copper and 70:30 brass from wire drawing, compression, and torsion. *Metall. Trans.* A **20**, 125–131.

Stout, M. G., Kallend, J. S., Kocks, U. F., Przystupa, M. A. & Rollett, A. D. 1988 Material dependence of deformation texture development in various deformation modes. In *Proc. 8th Int. Conf. Textures of Materials* (ed. J. S. Kallend & G. Gottstein), pp. 479–484. Warrendale, PA: The Metallurgical Society.

Taylor, G. I. 1938 Plastic strain in metals. *J. Inst. Met.* **62**, 307–324.

Tiem, S., Berveiller, M. & Canova, G. R. 1986 Grain shape effects on the slip system activity and on the lattice rotations. *Acta Metall.* **34**, 2139–2149.

Tomé, C. N. & Canova, G. R. 1998 Self-consistent modeling of heterogeneous plasticity. In *Texture and anisotropy: preferred orientations in polycrystals and their effects on material properties* (ed. U. F. Kocks, C. N. Tomé & H. R. Wenk), pp. 467–509. Cambridge University Press.

Tomé, C. N., Lebensohn, R. A. & Kocks, U. F. 1991 *Acta Metall. Mater.* **39**, 2667–2680.

Toth, L. S., Neale, K. W. & Jonas, J. J. 1989 Stress response and persistence characteristics of the ideal orientations of shear textures. *Acta Metall.* **37**, 2197–2210.

van Houtte, P. 1978 Simulation of the rolling and shear texture of brass by the Taylor theory adapted for mechanical twinning. *Acta Metall.* **26**, 591–604.

van Houtte, P. & Aernoudt, E. 1976 Considerations on the crystal and the strain symmetry in the calculation of deformation textures with the Taylor theory. *Mater. Sci. Engng* **23**, 11–22.

Wasserman, G. 1963 Der Einflußmechanischer Zwillingsbildung auf die Entstehung der Walztexturen Kubisch Flächenzentrierter Metalle. *Z. Metallk.* **54**, 61–65.

Wenk, H. R., Matthies, S., Donovan, J. & Chateigner, D. 1998 BEARTEX: a windows-based program system for quantitative texture analysis. *J. Appl. Cryst.* **31**, 262–269.

Williams, R. O. 1962 *Trans. Metall. Soc. AIME* **224**, 129.

Young, C. T., Steele, J. H. & Lytton, J. L. 1973 Characterization of bicrystals using Kikuchi patterns. *Metall. Trans.* **4**, 2081–2088.